Journal of the Mechanics and Physics of Solids 139 (2020) 103938

Contents lists available at ScienceDirect

Journal of the Mechanics and Physics of Solids

journal homepage: www.elsevier.com/locate/jmps

# Mechanics of bacteria-assisted extrinsic healing

An Xin, Haixu Du, Kunhao Yu, Qiming Wang*

*Sonny Astani Department of Civil and Environmental Engineering, University of Southern California, Los Angeles, CA 90089, United States*

ARTICLE INFO

*Article history:*
Received 4 November 2019
Revised 23 January 2020
Accepted 10 March 2020
Available online 19 March 2020

*Keywords:*
Self-healing mechanics
Microbial precipitation
Crystal growth
Cohesive zone model

ABSTRACT

Self-healing materials can typically be divided into two types: intrinsic healing that harnesses dynamic bones to autonomously repair fractures, and extrinsic healing that uses the externally added components to enable the bonding of fractured interfaces. Although the theoretical modeling of intrinsic self-healing materials has been recently studied by Wang et al., the fundamental understanding and theoretical modeling of the extrinsic self-healing materials remain elusive. Without a deep understanding of the extrinsic healing mechanics, the design of extrinsic-healing materials and corresponding applications are still at the trial-and-error stage. Here, taking bacterial-precipitation-enabled healing as an example, we construct a modeling framework to explain the bacteria-assisted extrinsic healing mechanics. A model for the growth of crystal pillars is developed to explain the bacteria-assisted growth of the calcium carbonate ($CaCO_3$) crystal forest within the fracture interface, and a cohesive zone model is built to explain the interfacial bonding. Our modeling framework can explain the evolution of the interfacial healing strength over the healing time and reveal the effects of interface distance and concentrations of bacteria and calcium ions on the healing performance. The modeling results are consistent with the bacteria-assisted healing experiments of ceramics and cement.



## 1. Introduction

Self-healing materials are synthetic materials that have special ability to repair fractures without human interventions (Binder, 2013; Li et al., 2018; Roy et al., 2015; Taylor, 2016; Thakur and Kessler, 2015; van der Zwaag, 2007; Wei et al., 2014; Wojtecki et al., 2011; Wu et al., 2008; Yang and Urban, 2013). Self-healing materials have been used in a broad range of applications, including flexible electronics (Tee et al., 2012), energy storage (Wang et al., 2013b), biomaterials (Brochu et al., 2011), and robotics (Terryn et al., 2017). Self-healing materials are typically divided into two types: The first type is "intrinsic self-healing material" that features dynamic bonds that can autonomously reform once fractured material parts are brought into contact. These dynamic bonds have been widely studied in soft polymer systems, such as dynamic covalent bonds (Chen et al., 2002; Ghosh and Urban, 2009; Imato et al., 2012; Lu and Guan, 2012; Skene and Lehn, 2004), hydrogen bonds (Chen et al., 2012; Cordier et al., 2008; Montarnal et al., 2009; Phadke et al., 2012; Sijbesma et al., 1997; Wang et al., 2013a), ionic bonds (Das et al., 2015; Haraguchi et al., 2011; Ihsan et al., 2016; Mayumi et al., 2016; Sun et al., 2012, 2013; Wang et al., 2010), metal-ligand coordination (Burnworth et al., 2011; Holten-Andersen et al., 2011; Kersey et al., 2007; Nakahata et al., 2011; Rowan and Beck, 2005; Wang et al., 2013b), host-guest interactions (Liu et al., 2017a, 2017b), hydrophobic interactions (Gulyuz and Okay, 2014; Okay, 2015), and $\pi$-$\pi$ stacking (Fox et al., 2012). The characteristic of

* Corresponding author.
*E-mail address:* qimingw@usc.edu (Q. Wang).

https://doi.org/10.1016/j.jmps.2020.103938
0022-5096/

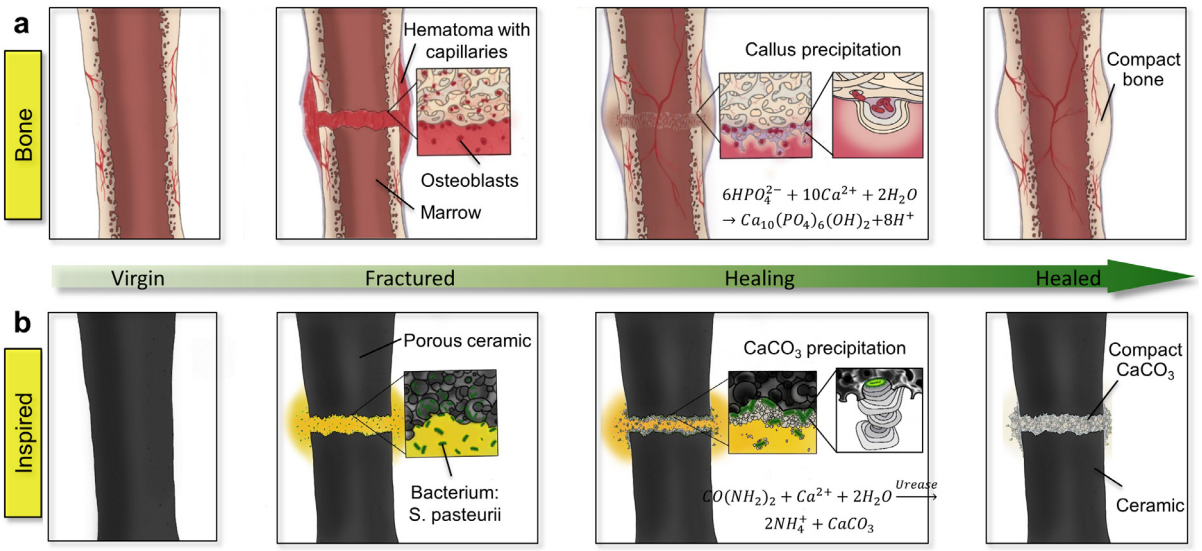


**Fig. 1.** Bioinspired concept of bacteria-assisted extrinsic healing. (a) Schematics for the healing process of a fractured human bone enabled by osteoblast-induced precipitation of callus. (b) Schematics for the healing process of a fractured ceramic bone enabled by bacteria-assisted precipitation of $CaCO_3$.

the intrinsic self-healing material is that the microstructure of the healed material resembles that of the virgin material. The second type is "extrinsic self-healing material" that harnesses the externally added components to enable the bonding of fractured interfaces. The externally added components include encapsulates of curing agents that can be released upon fractures (Blaiszik et al., 2010; Cho et al., 2006; Keller et al., 2007; Toohey et al., 2007; White et al., 2001), healing agents that can be activated to heal ceramics at high temperature (>1000 °C) (Ando et al., 2002, 2001; Chu et al., 1995; Li et al., 2012; Osada et al., 2017; Raj et al., 2014; Sloof et al., 2016; Song et al., 2008), and microorganism-assisted crystal precipitations that can bond the fracture interfaces of cementitious materials (Achal and Mukherjee, 2015; Jonkers et al., 2010; Luo et al., 2018; Nguyen et al., 2018; Wang et al., 2014). Different from the intrinsic healing materials, the materials within the healing interface region may be different from that of the virgin material. This extrinsic healing paradigm is typically used for traditionally unhealable stiff materials, such as rigid polymers, ceramics, and cement.

Despite the rich experimental studies of various extrinsic self-healing materials, the theoretical modeling of the self-healing mechanics is still at the incipient stage. Although the theoretical modeling of intrinsic healing materials has been recently studied by Wang et al. (2017), Xin et al. (2019), Yu et al. (2019a), (2018), (2019b), the fundamental understanding and theoretical modeling of the extrinsic healing materials remain elusive. Without a deep understanding of the extrinsic healing mechanics, the design of extrinsic-healing materials and the corresponding applications are still at the trial-and-error stage. In order to reveal the mechanism and guide future applications, a theoretical understanding of extrinsic healing mechanics is highly desired.

Here, we consider a class of extrinsic healing behavior that is enabled by bacteria-assisted crystal precipitation. This paradigm has been used to heal cementitious materials (Achal and Mukherjee, 2015; Jonkers et al., 2010; Luo et al., 2018; Nguyen et al., 2018; Wang et al., 2014). We here employ bacteria-assisted crystal precipitation to enable the healing of structured ceramics. This new technology has three outstanding advantages: (1) This paradigm is compatible with 3D-printed ceramics. Emerging additive manufacturing technology brings a leap to the ceramic field by enabling rapid prototyping of free-form ceramic architectures (Eckel et al., 2016; Halloran, 2016; Jang et al., 2013; Meza et al., 2014; Muth et al., 2017; Zanchetta et al., 2016a; Zocca et al., 2015) for applications as diverse as machine engines (Padture et al., 2002), energy storage devices (Li et al., 2016), biomedical devices (Park and Lakes, 2007), water membranes (Low et al., 2017), and body armor (Pugh and Pugh, 1971). Despite the great potential, a longstanding challenge is that 3D-printed ceramics typically feature low tolerance to damages and fractures (Eckel et al., 2016; Halloran, 2016; Jang et al., 2013; Meza et al., 2014; Muth et al., 2017; Zanchetta et al., 2016a; Zocca et al., 2015). This new healing paradigm is expected to significantly improve the damage tolerance of the 3D-printed ceramic structures. (2) This paradigm enables the healing of ceramics at room temperature. Existing healable bulk ceramics primarily rely on oxidation or re-sintering at high temperatures (>1000 °C) (Ando et al., 2002, 2001; Chu et al., 1995; Li et al., 2012; Osada et al., 2017; Raj et al., 2014; Sloof et al., 2016; Song et al., 2008). The high-temperature requirement precludes any *in situ* or autonomous healing of ceramics that operate at low temperatures, such as biomedical devices (Park and Lakes, 2007), water membranes (Low et al., 2017), and body armor (Pugh and Pugh, 1971). The room-temperature healing may drastically expand the practical application potential of self-healable ceramics. (3) This paradigm highlights the potential for creating biomimetic bones with self-healing capability. The healing of a fractured human bone relies on stem cells called *osteoblasts* to precipitate mineralized calluses (primarily $Ca_{10}(PO_4)_6(OH)_2$) to bridge fracture interfaces at body temperature (Fig. 1a) (Guan et al., 2012; Schindeler et al., 2008; Taylor et al., 2007). Inspired by

bones, we here employ bacteria (i.e., *Sporocarcina pasteurii*) as artificial osteoblasts to enable interfacial healing of ceramics at room temperature (Fig. 1b).

The process of the bacterial-precipitation-enabled healing of ceramics is hypothesized as two steps: In step 1, the bacteria-assisted nucleation and growth of crystals (i.e., $CaCO_3$) within the fracture interface region with a small interface gap (e.g., 300 $\mu$m). In step 2, the bacteria-assisted precipitation enables strong bonding to bridge the fracture interface, eventually leading to a healed interface with an interfacial strength comparable to the strength of the virgin ceramic material. Here, we develop a modeling framework to explain these two steps for the bacteria-assisted healing of ceramics: We employ a model for the growth of crystal pillars to explain the bacteria-assisted growth of the $CaCO_3$ crystal forest within the fracture interface, and a cohesive zone model to explain the interfacial bonding. Our modeling framework can eventually explain the evolution of the interfacial healing strength over the healing time. The modeling results are consistent with the bacteria-assisted healing experiments of ceramics and cement.

The plan of this paper is as follows. In Section 2, the experimental procedures and results for the bacteria-assisted healing of ceramics and cement are presented. In Section 3, we construct the modeling framework which includes the bacteria-assisted production of solute $CaCO_3$, nucleation and growth of crystal pillars, and cohesive modeling of the healed interface. In Section 4, we show the theoretically calculated results of the models and discuss the effects of healing interface distance, bacterial concentration, and calcium ions on the healing performance. Section 5 will illustrate the comparison between the theoretical and experimental results. The conclusive remarks are presented in Section 6.

## 2. Experimental procedures and results

Poly (methyl-silsesquioxane) (MK) powders were purchased from Gelest. Tetrahydrofuran (THF), tri (propylene glycol) methyl ether (DOWANOL), 3-(Trimethoxysilyl) propyl methacrylate (TMSPM), phenylbis (2,4,6-trimethylbenzoyl) phosphine oxide (photoinitiator), Sudan I (photo absorber), and ethanol were all purchased from Sigma-Aldrich. 48-μm polymethylmethacrylate (PMMA) powders were purchased from Goodfellow. Hydrochloric acid was purchased from GR ACS. The MK-TMSPM resin was prepared same as described in Zanchetta's paper (Zanchetta et al., 2016b). 18 g PMMA was mixed with 30 g resin by stirring for 2 h. Besides, 1.5 g PI and 0.03 g Sudan I were added and mixed well by stirring for another 20 min to obtain the photocurable preceramic polymer. The photopolymerization experiments were performed with a projection stereolithography system. Rectangular samples were printed with a dimension of 24mm × 8mm × 2mm. Samples were dried in air at room temperature for 24 h and subsequently pyrolyzed in a tube furnace (Thermo Scientific Lindberg/Bule M TF55030A). The furnace temperature was programmed to increase from 25 to 350 °C over 3 h 30 min and then keep at 350 °C for 1 h in airflow. The furnace was continuously heated up from 350 to 1000 °C over 10 h and then kept at 1000 °C over 1 h in a nitrogen atmosphere (99.998%). Finally, the furnace was cooled from 1000 to 25 °C over 4 h 30 min in a nitrogen atmosphere. Porous ceramic samples were manufactured via thermal degradation of PMMA and pyrolysis of the MK-TMSPM network.

The cement clinker used in the current research was purchased from Pure Organic Ingredients. Cement paste samples were prepared at the w/c (DI water/cement) of 0.5 (Li et al., 2004). The well-mixed cement paste was injected into rectangular molds (16.8mm × 5.6mm × 1.2mm) and cured for 4 days in a certain atmosphere (temperature of 25 °C and relatively humidity of around 90%) which was controlled by an incubator.

*Sporosarcina pasteurii* (ATCC 11859, non-infectious) was purchased from American Type Culture Collection (ATCC). Tryptone, ammonium sulfate, ammonium chloride, sodium bicarbonate, and calcium chloride were purchased from Sigma-Aldrich. Urea, tricine, yeast extract, agar, and L-glutamic acid were purchased from Alfa Aesar, to prepare the BPU medium (ATCC 1832) and the urea-$CaCl_2$ medium. Difco nutrient broth was purchased from Fisher Scientific. All chemicals were used without further purification. The medium preparation has been described in other papers (Bang et al., 2001; Stocks-Fischer et al., 1999). *Sporosarcina pasteurii* was inoculated and grown in the solid BPU medium for two days at 30 °C.

Both porous ceramic samples and cement samples were soaked in 150 ml BPU medium with bacteria for 24 h at 30 °C (Fig. 2ab). The cell concentration in the growth medium is around $0.8 \times 10^8$ ~$1.4 \times 10^8$ cells/ml, which was determined by reading the optical density at 600 nm (Thermo Scientific NanoDrop UV–VIS Spectrophotometer). The purpose of the presoaking was to attach the bacteria to the surface of the ceramic pores. The surface-attached bacteria serve as the nucleation sites for the crystal precipitation. A three-point-bending load was applied to break the samples into two parts (Fig. 2c) and the original strength was tested concurrently. The fractured structures were fixed tightly with glass supports and VHB tapes leaving around 300 μm-wide cracks between the two broken parts (Fig. 2d). The interfacial gap (300 μm) is set to enable the interfacial bridging with the precipitated crystals. After then, the fixed structures were immersed in 150 ml urea-$CaCl_2$ medium and kept in an incubator at 25 °C (Fig. 2e). This precipitation medium was refreshed every 24 h. Certain quantities of bacteria were moved from microbial culture into the newly added medium via warmed inoculating loop to achieve a specific cell concentration (~$1.0 \times 10^8$ cell/mL). Three-point bending (3PB) tests were carried out on these treated samples using an Instron mechanical tester (Model 5942) every two days from day 0 to day 14. The time-varying sample surface was recorded with a camera (Canon EOS 70D). The interfacial microstructures, bacteria, and precipitations of ceramic samples were imaged using an scanning electron microscope (SEM) (JEOL JSM-7001).

During the healing process, precipitated $CaCO_3$ crystals gradually grew and eventually formed bridges between the fracture interfaces (Fig. 3ab). This was further confirmed by interfacial SEM images: both size and surface coverage of the adhered crystal particles increased over days (Fig. 3c). The healing strengths of the healed ceramics were further charac-

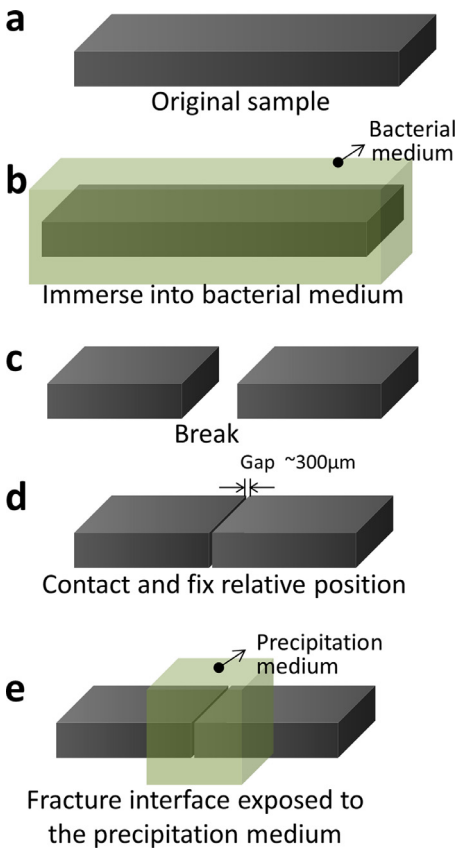


**Figure 2.** Experimental process of the bacteria-induced interfacial healing of ceramics. The sample was first immersed into a medium containing urease-producing bacteria *Sporosarcina pasteurii* for 24 h to enable the bacteria to attach to pore surfaces (a-b). Then the sample was broken into two parts (c). Two fractured pieces were brought into contact with a very small gap distance (~300 μm) and the relative position was fixed with glass supports and VHB tapes (d). Finally, the fracture interface was exposed to a precipitation medium (e).

terized by 3PB tests (Fig. 3d). It was found that the maximum loads of the 3PB tests increased over days until reaching a plateau which was around the maximum load of the virgin ceramic. We then calculated the effective flexural strength of the healed interface and normalized it with virgin flexural strength to obtain the healing strength ratio. The healing strength ratio increased with the healing time and reaches a plateau around 100% after 10 days (Fig. 3e).

Cement samples were immersed in the urea-$CaCl_2$ medium as the experimental process of ceramic samples (Fig. 4a). Visibly, the crack on the surface was gradually covered by $CaCO_3$ precipitation over days (Figs. 4b). The crack was clearly visible at the beginning, but blurrier over days. Similarly, a plateau of the healing strength of cement samples was obtained after 10 days (Fig. 4cd).

## 3. Modeling framework

In this section, we will establish a modeling framework to understand the mechanism of the microbial precipitation induced interfacial bonding. The model will be able to explain the mechanisms of the following three processes: (1) The bacteria-assisted chemical reaction produces solute calcium carbonates ($CaCO_3$). (2) Once the solute calcium carbonates are oversaturated in the solution, they will precipitate as solid crystals initiated by the bacteria bonded on the solid surface. The precipitated crystals will grow over time to bridge the interfacial gap of the fracture. (3) When the bridged/healed sample undergoes a 3PB test, the healed interface fractures when the load is large enough. In process 1, the model primarily covers the chemical kinetics for the formation of solute calcium carbonates. In process 2, the model will explain the nucleation and growth process of the precipitation. In process 3, the model addresses the interfacial fracture problem of the healed sample under the 3PB load.

Although the microbially-induced mineral precipitation has been modeled in sand systems (Barry, 2018; Ebigbo et al., 2012; Hommel et al., 2015), these studies are primarily focused on the precipitation of isolated crystal particles within the solution. It is still elusive how to model the growth of the microbial precipitation and how to connect the precipitation growth to the healed interfacial strength. Here, we overcome these technical barriers by developing a modeling framework to quantitatively relate the interfacial healing strength and the healing time.

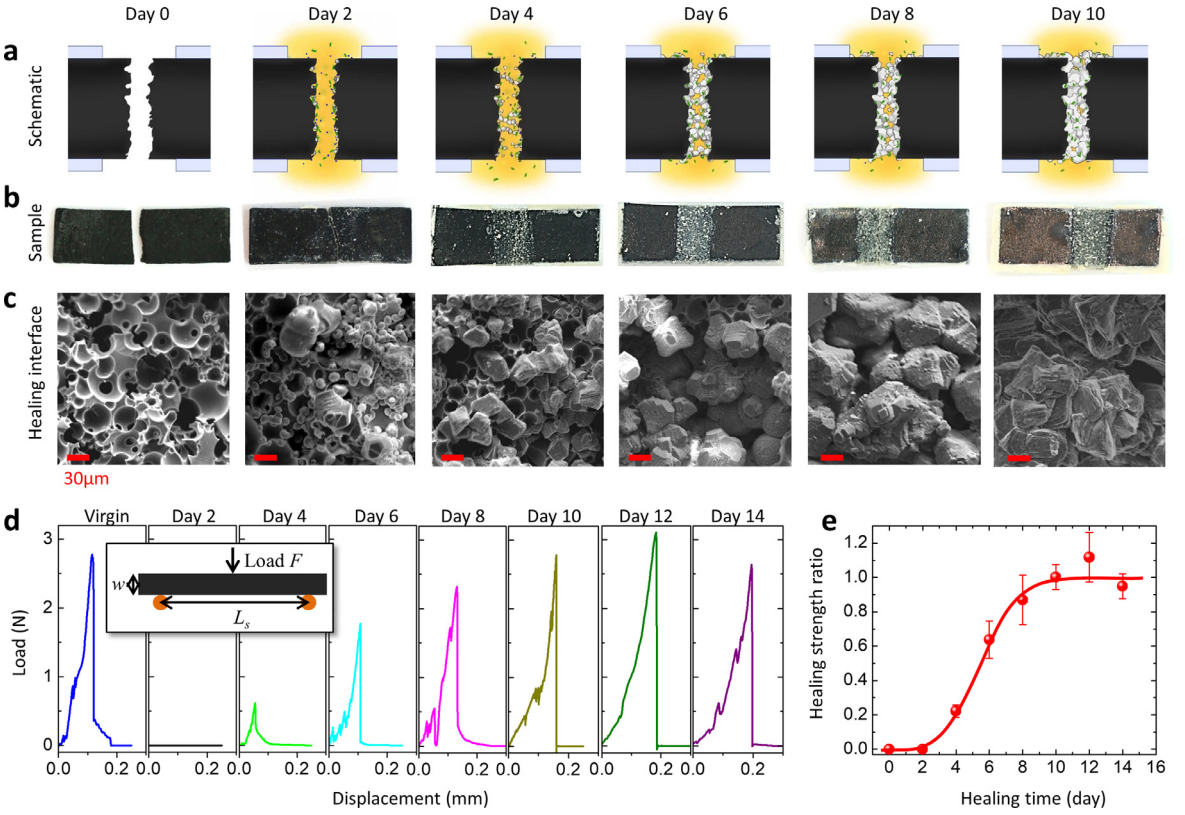


**Fig. 3.** Experiments of bacteria-assisted healing of ceramics. (a) Schematics of nucleation and growth of bacteria-assisted precipitation of $CaCO_3$ crystals on the fracture interface over 10 days. (b) Healing of ceramic plate samples (length 17 mm, width 5.68 mm, and thickness 1.42 mm) over 10 days. (c) SEM images of healing interfaces of ceramic plate samples over 10 days. (d) Load-displacement curves of virgin and healed samples over 10 days in 3PB tests. The inset shows the schematic for the 3PB test, where $F$ is applied load, $L_s$ is span between two supporting points, and $w$ is sample thickness. (e) Healing strength ratios of ceramic plates as a function of healing time. Healing strength ratio is defined as the effective flexural strength of healed samples normalized by that of the virgin sample.

### 3.1. Bacteria-assisted production of solute calcium carbonates

The chemical reactions related to the production of solute calcium carbonates ($CaCO_3$) are shown in Fig. 5a (Barry, 2018; Ebigbo et al., 2012; Hommel et al., 2015). First, the urea ($CO(NH_2)_2$) activated by the bacteria-produced enzyme urease undergoes a ureolysis reaction to produce the ammonium and carbonate ions. The carbonate ions then react with calcium ions to form solute $CaCO_3$. In the beginning, the urea, calcium ions, and bacteria are given with initial concentrations as $C^0_{urea}$, $C^0_{Ca^{2+}}$, and $C^0_{bacteria}$, respectively. During the process, the concentration of the urea, calcium ions, and bacteria decreases to produce the solute $CaCO_3$ which is precipitated out as crystal solids if proper condition is given.

The urease-catalyzed decomposition of urea can be explained by the Michaelis-Menten kinetics (Johnson and Goody, 2011; Krajewska, 2009), written as

$$\frac{\partial C_{urea}}{\partial t} = -\frac{k_{cat} C_{urease} C_{urea}}{C_{urea} + K_M} \tag{1}$$

where $C_{urea}$ is the concentration of urea (mol/L), $C_{urease}$ is the concentration of urease (mol/L), $k_{cat}$ is the catalytic rate ($s^{-1}$), and $K_M$ is the Michaelis constant (mol/L). The enzyme urease is produced by the bacteria, governed by (Sarda et al., 2009)

$$\frac{\partial C_{urease}}{\partial t} = k_b C_{bacteria} \tag{2}$$

where $k_b$ is the production rate (mol/L/s/(cell/mL)) and $C_{bacteria}$ is the bacterial concentration (cell/mL).

We consider the production of the $CaCO_3$ is an irreversible reaction with the changing rate of the calcium ions written as (Reddy and Gaillard, 1981)

$$\frac{\partial C_{Ca^{2+}}}{\partial t} = -k_c C_{Ca^{2+}} C_{CO_3^{2-}} \tag{3}$$

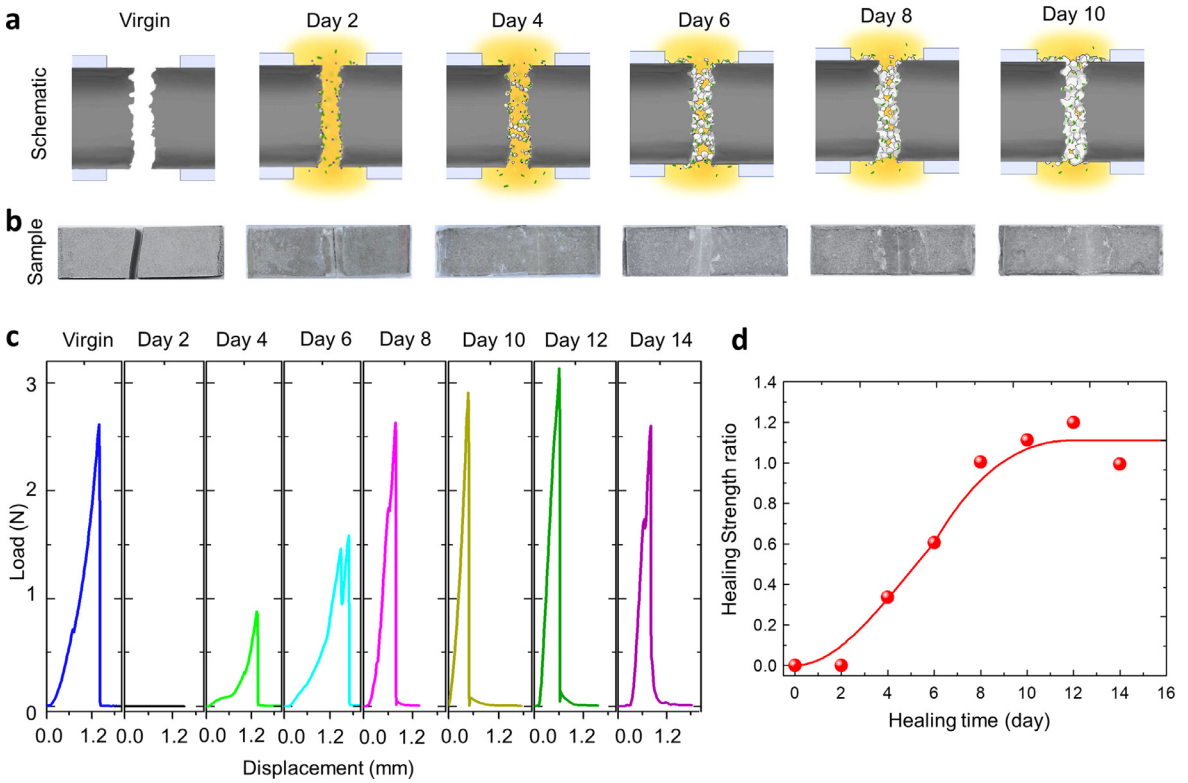


**Fig. 4.** Experiments of bacteria-assisted healing of cement. (a) Schematics of nucleation and growth of bacteria-assisted precipitation of $CaCO_3$ crystals on the fracture interface over 10 days. (b) Healing of cement plate samples over 10 days (c) Load-displacement curves of virgin and healed samples over 10 days in 3PB tests. (d) Healing strength ratios of ceramic plates as a function of healing time. Healing strength ratio is defined as the effective flexural strength of healed samples normalized by that of the virgin sample.

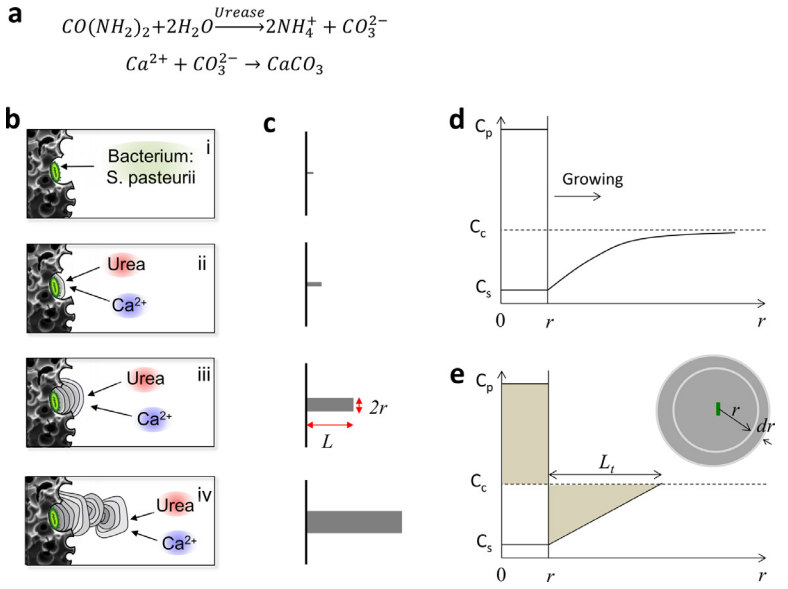


**Fig. 5.** Model system for the growth of a pillar. (a) Chemical reactions for the production of solute $CaCO_3$. (b) Schematics to show bacteria-assisted nucleation and growth of $CaCO_3$ crystals on a ceramic surface. (c) Simplified pillar model for the crystal. (d) The diffusion-controlled growth of a precipitated crystal particle. $C_p$ is the concentration of the solute in the precipitate. $C_c$ is the concentration of the solute in the solution. $C_s$ is the concentration of the solution after precipitation. (e) Simplification of the concentration profile.

where $C_{Ca^{2+}}$ is the concentration of the calcium ions (mol/L), $C_{CO_3^{2-}}$ is the concentration of the carbonate ions (mol/L), and $k_c$ is the reaction rate (1/s/(mol/L)). The concentration of the calcium ions is given in the initial state, and then decreases during the reaction. The carbonate ions are produced during the decomposition of urea and consumed by the reaction between the carbonate ions and calcium ions. Therefore, the changing rate of $C_{CO_3^{2-}}$ can be calculated as

$$\frac{\partial C_{CO_3^{2-}}}{\partial t} = \frac{k_{cat} C_{urease} C_{urea}}{C_{urea} + K_M} - k_c C_{Ca^{2+}} C_{CO_3^{2-}} \tag{4}$$

At the initial state, the concentration of the bacteria is given. During the one-day process, the concentration of bacteria decreases because high concentrations of carbonate ions and calcium ions are not pleasant living conditions for the bacteria. The changing rate of the bacteria can be roughly modeled as (Juška et al., 2006; Teleken et al., 2011; Zwietering et al., 1990)

$$\frac{\partial C_{bacteria}}{\partial t} = -k_d C_{bacteria} C_{Ca^{2+}} C_{CO_3^{2-}} \tag{5}$$

where $k_d$ is the bacterial death rate (1/s/(mol/L)$^2$).

If we assume the initial concentration of the urea ($C^0_{urea}$) is higher than that of the calcium ions ($C^0_{Ca^{2+}}$), the concentration of produced solute $CaCO_3$ can be calculated as

$$C_C = C^0_{Ca^{2+}} - C_{Ca^{2+}} \tag{6}$$

where $C_C$is the concentration of produced solute $CaCO_3$ (mol/L). Note that the accumulation of the solute $CaCO_3$ does not preclude the formation of the solute $CaCO_3$, because the production of $CaCO_3$ is modeled as an irreversible reaction. The concentration of solute $CaCO_3$ is actually a fictitious concentration value because solute $CaCO_3$ with high enough concentration will be precipitated as a crystal solid (see Section 3.2). Since the production of $CaCO_3$ is modeled as an irreversible reaction, the precipitation of $CaCO_3$ crystals does not affect the chemical kinetics to produce the solute $CaCO_3$.

### 3.2. Nucleation and growth of crystals

The precipitation process can be considered as follows. Bacteria *S. pasteurii* first grow within the porous ceramic and attach to the pore surface (Fig. 5bi). Once the ceramic is fractured and adequate precipitation chemicals (e.i., urea and $Ca^{2+}$) are delivered to the fracture location, bacteria produce an enzyme called *urease* which decomposes urea to initiate the nucleation of $CaCO_3$ crystals around the bacteria (Figs. 5bii) (De Muynck et al., 2010; Li et al., 2018). Then crystals gradually grow to cover the bacteria and bond on the ceramic surface. The crystals then grow into larger particles (Fig. 5biii), and new crystals nucleate and grow on the existing crystal particles to form a pillar-like structure, eventually bridging the fracture interface (Fig. 5biv).

The nucleation of the crystals is heterogeneous nucleation with the nucleation rate (number of nuclei per unit area and per second) written as (Porter et al., 2009)

$$\dot{N}_{het} = \omega C_1 \exp\left(\frac{\Delta G_m}{k_B T}\right) \exp\left(\frac{\Delta G^*_{het}}{k_B T}\right) \tag{7}$$

where $\Delta G_m$is the activation energy for the atomic migration, $\omega$is a factor to consider the vibration frequency of the atoms, $C_1$ is the concentration of heterogeneous nucleation sites per unit volume, $k_B$ is Boltzmann constant, and $T$ is the temperature. $\Delta G^*_{het}$ is the energy barrier for the heterogeneous nucleation, and can be expressed as (Porter et al., 2009)

$$\Delta G^*_{het} = \frac{(2+\cos\theta)(1-\cos\theta)^2}{2}\left(\frac{16\pi\gamma^3}{3\Delta G_v^2}\right) \tag{8}$$

where $\Delta G_v$ is the free energy reduction per unit volume during the precipitation process, $\gamma$ is the interfacial energy, and $\theta$ is the wetting angle between the liquid and solid phases. According to Eqs. (7) and (8), the nucleation rate is a linear relationship of the concentration of the heterogeneous nucleation sites. As shown in Fig. 5b, the attached bacteria provide the nucleation sites. We here make a bold assumption that the attached bacteria should be a linear relationship with the bacteria concentration $C_{bacteria}$ within the medium. Therefore, we conclude that the nucleation rate is a linear relationship with the bacteria concentration, written as

$$\dot{N}_{het} = \frac{\partial N_{net}}{\partial t} = k_u C_{bacteria} \tag{9}$$

where $k_u$ is a constant parameter ($s^{-1}$).

Next, we consider the growth of the precipitation (Fig. 5c). We here first consider the growth of pillar-like precipitation. During the growth, both the radius $r$ and length $L$ of the crystal pillar increase. Let us first consider an intermediate state to depict the growth of the radius $r$. Physically, the concentration of soluble $CaCO_3$ in the water (denoted as $C_s$) is very low (0.013 g/L) (Tegethoff et al., 2001); however, the concentration of solute $CaCO_3$ $C_C$ is usually much higher than $C_s$. When the solution is in the oversaturated state, the $CaCO_3$ will precipitate as crystals. Bacteria provide nuclei for the $CaCO_3$

precipitation (Balluffi et al., 2005; Porter et al., 2009). The $CaCO_3$ crystal is expected to first nucleate around the bacteria sites and then gradually grow out to fill the fracture gap.

The precipitation growth in the radius can be understood as follows with a schematic in Fig. 5d. The substrate is located at $r = 0$, and the precipitation front is at $r$. Within the area 0–$r$ is in the precipitation state with the molar concentration of $CaCO_3$ within the solid precipitation as $C_p$. Right at precipitation front $r^+$, the molar concentration of solute $CaCO_3$ is $C_s$; while at the location far from the precipitation front, the molar concentration of solute $CaCO_3$ is $C_c$. The molar concentration profile of $CaCO_3$ around the precipitation front is shown in Fig. 5d. Considering the front moves by a small distance $dr$ within a small time $dt$, the number of $CaCO_3$ atoms needed for such a movement is given by

$$dN = (C_p - C_s)(2\pi r)drdz \tag{10}$$

where $dz$ is a segment length along the pillar length. Since $CaCO_3$ atoms are supplied to the front by diffusion, using the Fick's first law, we can estimate the number of $CaCO_3$ atoms that diffuse in time $dt$ as

$$dN = D(2\pi rdz)\frac{\partial C}{\partial r}dt \tag{11}$$

where $D$is the diffusion coefficient of $CaCO_3$ atoms within the solution and $C(r, t)$is the concentration of solute $CaCO_3$ at location $r$ and at time $t$. Equating the quantities $dN$ in Eqs. (10) and (11), we obtain the movement velocity as (Balluffi et al., 2005; Porter et al., 2009; Zener, 1949)

$$\frac{dr}{dt} = \frac{D}{C_p - C_s}\frac{\partial C}{\partial r} \tag{12}$$

To estimate $\partial C/\partial r$ in Eq. (12), we consider a simplified concentration profile shown in Fig. 5e. The concentration gradient can be estimated as

$$\frac{\partial C}{\partial r} \approx \frac{C_c - C_s}{L_t} \tag{13}$$

where $L_t$ is the effective length of the concentration tail. Using the conservation of mass between the two shadow areas in Fig. 5e, we obtain

$$\left(\pi r^2 dz\right)(C_p - C_c) = \pi\left[(L_t + r)^2 - r^2\right]dz\left(\frac{C_c - C_s}{2}\right) \tag{14}$$

We thus can obtain $L_t$ as

$$L_t = r\left[\sqrt{\frac{2C_p - C_c - C_s}{C_c - C_s}} - 1\right] \tag{15}$$

Integrating Eqs. (15), (13), and (12), we obtain

$$\frac{dr}{dt} = \frac{D}{C_p - C_s}\frac{C_c - C_s}{r\left[\sqrt{\frac{2C_p - C_c - C_s}{C_c - C_s}} - 1\right]} \tag{16}$$

Since $C_s < < C_c$and $C_s < < C_p$, we reduce Eq. (16) as

$$\frac{dr}{dt} = \frac{DC_c}{rC_p\left[\sqrt{\frac{2C_p - C_c}{C_c}} - 1\right]} \tag{17}$$

To link the pillar length and the radius, we employ the Zener–Hillert equation to model the growth of a pillar as (Hillert, 1957; Zener, 1946)

$$\frac{dL}{dt} = \frac{D}{4r}\frac{c_p - c_c}{c_c - c_s} \tag{18}$$

where $L$ is the pillar length. Since $C_s < < C_c$and $C_s < < C_p$, we reduce Eq. (18) as

$$\frac{dL}{dt} = \frac{D(c_p - c_c)}{4rc_c} \tag{19}$$

The initial condition for Eqs. (17) and (19) is

$$L(t = 0) \approx r(t = 0) = r_0 \tag{20}$$

where $r_0$ is the initial nuclei radius that can be appreciated as the average radius of bacteria. Integrating Eqs. (17), (19), and (20), we can fully solve the radius $r$ and length $L$ of the pillar during the growth process.

Once the nucleation and growth of a crystal pillar are understood, let us consider the group behavior of all crystal pillars on the fracture interface (Fig. 6a). When a pillar length $L$ is equal to the interface distance $L_g$, this pillar is expected to bridge

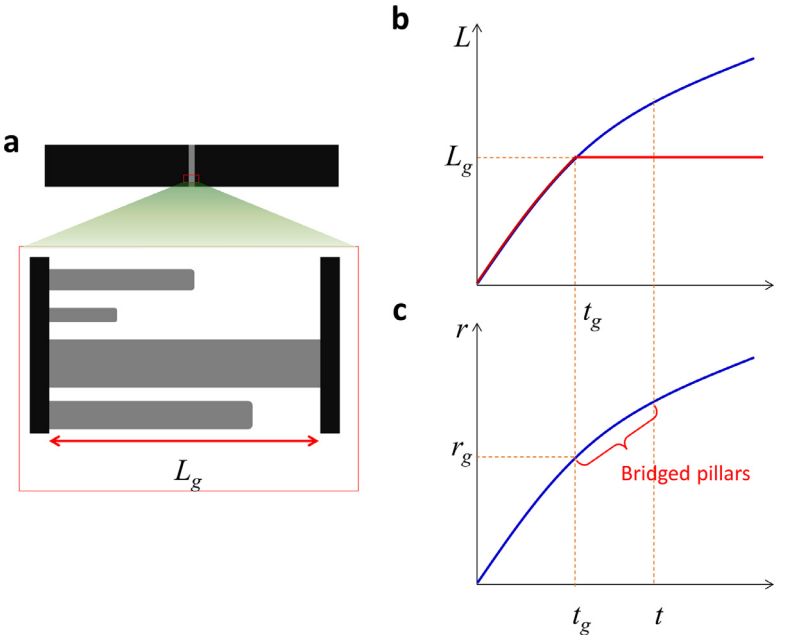


**Fig. 6.** Growth of pillar forest to bridge the fracture interface. (a) Schematic to show the pillar forest on the fracture interface. $L_g$ is the fracture interface distance. (b) Schematic to show the pillar length in a function of time. (c) Schematic to show the pillar radius in a function of time.

the interface. The corresponding time for the length $L(t) = L_g$ is $t_g$ (Fig. 6b). Before time $t_g$, no pillar bridges the interface, so the interfacial bonding is expected to be zero. After time $t_g$, the interfacial bonding becomes non-zero and begins to increase. The interfacial bonding increase is due to two factors: (1) More and more pillars attach cross the interface; and (2) the bridged pillars are becoming bigger in the radius. After $L(t) = L_g$, we here assume that radius expanding law still follows Eq. (17) (Fig. 6c), because the pillar radius is independent of the pillar length $L$ (revealed from Eq. (17)).

At time $t$ ($t > t_g$), the pillars bridging the interface can be considered as those nucleated during time 0 to $t - t_g$. Therefore, the total number of pillars bridging the interface per unit interface area can be written as

$$N_p(t) = \int_0^{t-t_g} \dot{N}_{net}(\tau)d\tau \tag{21}$$

These bridged pillars have different radii. The total cross-section area of the bridged pillars per unit interface area can be calculated as (Fig. 6c)

$$A(t) = \int_{t_g}^{t} \dot{N}_{net}(t-\tau)\pi r^2(\tau)d\tau \tag{22}$$

### 3.3. Cohesive modeling of the healed interface

After modeling the crystal growth on the healed interface, we study the interfacial strength of the healed interface. Under a sufficiently large load in the three-point-bending test, the healed interface may fracture in the following two modes: interfacial fracture between the crystals and ceramic and cohesive fracture within the crystals. To determine which mode dominates, we break the healed sample into two parts and find $CaCO_3$ crystals can be found on both fracture interfaces (Fig. 7). This evidence verifies that the bonding strength between the $CaCO_3$ crystals and the ceramic surface is stronger than the cohesive strength of the $CaCO_3$ crystals. Therefore, during the fracture of the healed region, the cohesive fracture of the bridged crystals dominates over the interfacial fracture between the crystals and the ceramic.

To model the interfacial strength of the healed interface, we consider the healed region as an effective continuum medium using a cohesive zone model (Fig. 8a) (Elices et al., 2002). A bilinear traction-separation law is employed, written as (Fig. 8b)

$$T_n = \begin{cases} \dfrac{S_h}{\delta_0}\delta_n, & 0 \le \delta_n \le \delta_0 \\ 2S_h - \dfrac{S_h}{\delta_0}\delta_n, & \delta_0 < \delta_n \le 2\delta_0 \end{cases} \tag{23}$$

where $T_n$ is the normal traction, $\delta_n$ is the normal separation displacement, $S_h$ is the normal cohesive strength, $2\delta_0$ is the maximal separation displacement. Considering the thickness of the cohesive zone as the fracture interface distance $L_g$, we

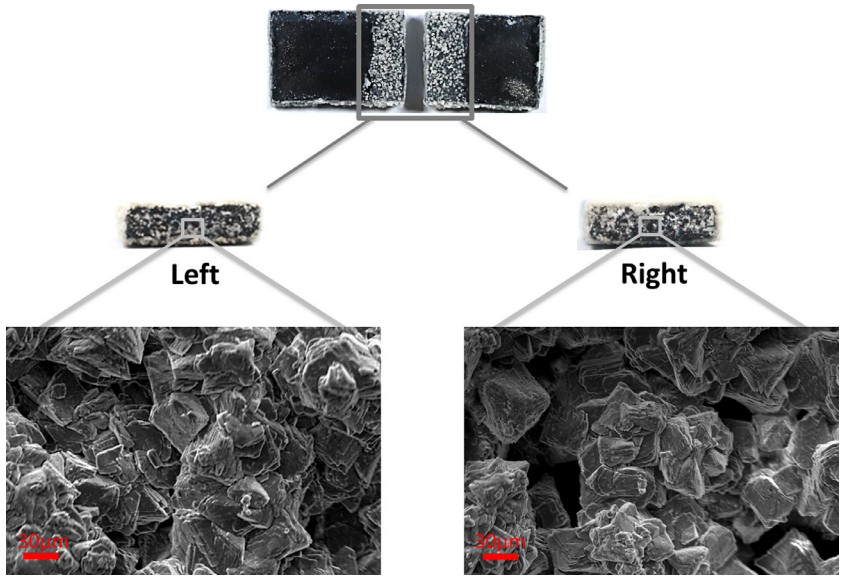


**Fig. 7.** A broken healed sample on day 10 and corresponding SEM images of two fracture interfaces.

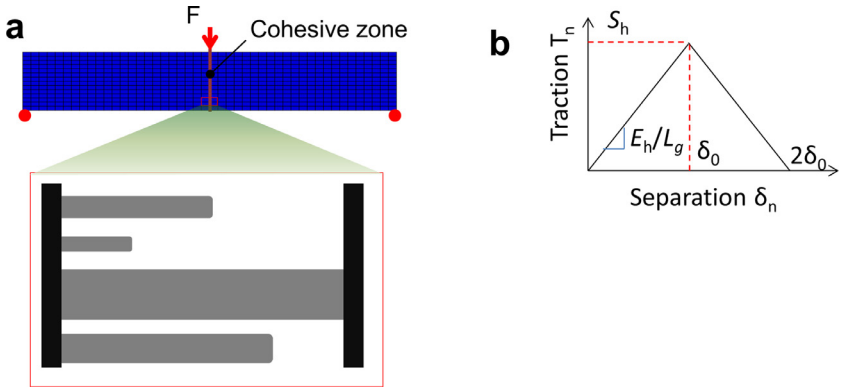


**Fig. 8.** (a) Cohesive zone model for the healed interface. (b) A bilinear traction-separation model for the cohesive zone.

can calculate the maximal separation displacement $2\delta_0$using Young's modulus of the cohesive zone $E_h$, written as (Fig. 8b)

$$\delta_0 = \frac{S_h}{E_h} L_g \tag{24}$$

Note that we here assume the damage initiation displacement is half of the maximum separation displacement. This assumption is to make sure that the cohesive zone model can be constructed with three governing parameters: Young's modulus of the cohesive zone $E_h$, The normal cohesive strength $S_h$, and the gap distance $L_g$. To model the damage initiation of the cohesive zone, we employ a quadratic stress criterion as

$$\left(\frac{t_n}{S_h}\right)^2 + \left(\frac{t_s}{S_h}\right)^2 = 1 \tag{25}$$

where $t_n$ and $t_s$ are nominal stresses on the crack surface in the normal and shear directions, respectively.

The normal cohesive strength $S_h$ and the Young's modulus $E_h$of the cohesive zone change during the crystal growth process. at the initial state, no crystal pillars bridge the fracture interface; and thus, the cohesive strength and the modulus are effectively zero. As more and more crystal pillars bridge the fracture interface, the cohesive strength becomes stronger and the effective stiffness of the healed region becomes larger. Here, we make a rough assumption that the cohesive strength and stiffness of the precipitated crystal remain the same during the whole crystal growth process, denoted as $S_0$ and $E_0$, respectively. Then, the healed region is modeled as a cellular solid composed of bridged crystal pillars and air (Gibson and Ashby, 1999). Here, the geometry of the cellular solid can be modeled as a simple parallel shape: crystal pillar

**Table 1**
Employed parameters in the paper. The estimation basis is given for each parameter.

| | Parameter | Physical meaning | Value | Basis |
|---|---|---|---|---|
| Parameters for healing | $C^0_{bacteria}$ (cell/mL) | Initial concentration of bacteria *Sporosarcina pasteurii* | $10^8$ | Experiment |
| | $C^0_{urea}$ (mol/L) | Initial concentration of urea | 0.33 | Experiment |
| | $C^0_{Ca^{2+}}$ (mol/L) | Initial concentration of calcium ions | 0.25 | Experiment |
| | $k_{cat}$ ($s^{-1}$) | Catalytic rate of urease | 3500 | (Johnson and Goody, 2011; Krajewska, 2009) |
| | $K_M$ (mol/L) | Michaelis constant | $1.8x10^{-2}$ | (Johnson and Goody, 2011; Krajewska, 2009) |
| | $k_b$ (mol/L/s/(cell/mL)) | Production rate of urease | $3x10^{-21}$ | (Sarda et al., 2009) |
| | $k_c$ (1/s/(mol/L)) | Reaction rate of calcium ions and carbonate ions | 400 | (Reddy and Gaillard, 1981) |
| | $k_d$ (1/s/(mol/L)$^2$) | Bacterial death rate | 1000 | (Juška et al., 2006; Teleken et al., 2011; Zwietering et al., 1990) |
| | $k_u$ ($s^{-1}$) | Nucleation rate parameter | $1.07x10^{26}$ | Fitting for Fig. 16b |
| | $C_p$ (mol/L) | Concentration of $CaCO_3$ within the solid precipitation | 0.6 | Fitting for Fig. 16a |
| | $D$ ($m^2$/s) | Diffusion coefficient of $CaCO_3$ atoms within the solution | $1x10^{-14}$ | (Grodzinsky, 2011) |
| | $L_g$ (μm) | Fracture interface gap distance | 300 | Experiment |
| | $S_0$ (MPa) | Cohesive strength of the precipitated crystal solid | 1.94 | Experiment |
| | $E_0$ (MPa) | Young's modulus of the precipitated crystal solid | 290 | Experiment |
| | $\gamma_h$ | Poisson's ratio of cohesive zone | 0.3 | Estimation for rigid solid |
| Parameters for ceramics | $E_{cer}$ (MPa) | Young's modulus of the employed porous ceramic | 175 | Experiment |
| | $\gamma_{cer}$ | Poisson's ratio of the employed porous ceramic | 0.3 | Estimation for rigid solid |
| Parameters for cements | $E_{cem}$ (MPa) | Young's modulus of the employed cement | 200 | Experiment |
| | $\gamma_{cem}$ | Poisson's ratio of the employed cement | 0.3 | Estimation for rigid solid |

and air phase are in parallel. Then, the effective strength and modulus of the cellular solid can be calculated as

$$S_h(t) = S_0 A(t) \tag{26}$$

$$E_h(t) = E_0 A(t) \tag{27}$$

where $A(t)$ is the cross-section area of the bridged pillars per unit interface area at healing time $t$, given by Eq. (22).

## 4. Modeling results

In this section, we present the modeling results for the bacteria-assisted production of the solution $CaCO_3$, the growth of crystals, and cohesive modeling of the healed interface. The evolution of the healing strength versus the healing time will be elucidated. Effects of fracture interface distance, bacterial concentration, and calcium ions on the healing strength evolution will be depicted.

### 4.1. Bacteria-assisted production of solute $CaCO_3$

To obtain the concentration of solute $CaCO_3$, we need to solve the differentiation equations in Section 3.1 (Eqs. (1)–(6)) with adequate initial conditions. According to the measurement from the Thermo Scientific NanoDrop UV–VIS Spectrophotometer, the concentration of the bacteria *Sporosarcina pasteurii* is in the order of $10^8$ cell/mL in the initial medium; thus, we assume $C^0_{bacteria} = 10^8$ cell/mL. The initial concentrations of urea and calcium ions in the precipitation medium are given as $C^0_{urea} = 0.33$ mol/L and $C^0_{Ca^{2+}} = 0.25$ mol/L, respectively. After 24 h (day 1), the precipitation medium will be refreshed: removing half volume of the old precipitation medium and adding half volume of the new precipitation medium. The initial conditions for day 2 should be updated by averaging the concentrations of bacteria, urea, calcium ions, and urease. Thereafter, the initial condition for each day should be updated accordingly.

With adequate reaction parameters (Table 1), we can calculate the evolution of the concentrations of bacteria, urease, calcium ions $Ca^{2+}$, and solute $CaCO_3$, shown in Fig. 9. Within the first 7 h of day 1, the bacterial concentration decreases from $10^8$ cell/mL to a plateau of $5.35 \times 10^7$ cell/mL (Fig. 9a), the calcium ions concentration decreases from 0.25 mol/L to 0 mol/L (Fig. 9c), and the solute $CaCO_3$ concentration increases from 0 to 0.25 mol/L (Fig. 9d). Within the rest 17 h of day 1, we assume all solute $CaCO_3$ can precipitate out as solid crystals, and the concentration of solute $CaCO_3$ returns to 0

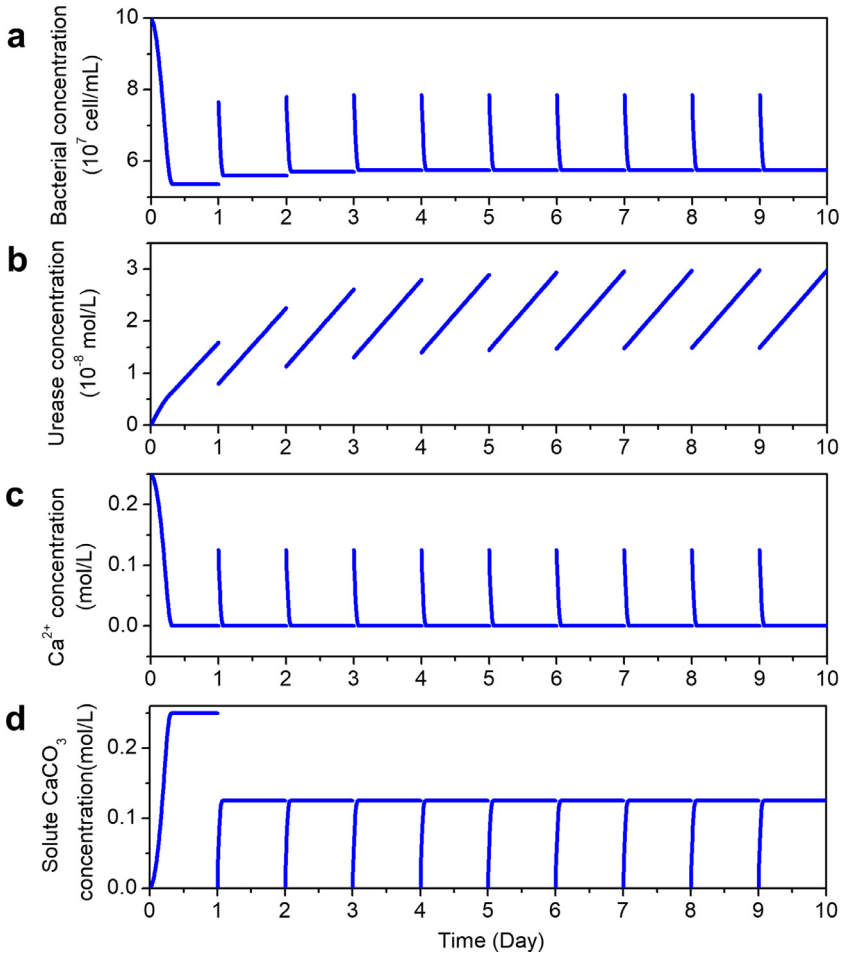


**Fig. 9.** Evolution of chemical concentrations over 10 days: (a) bacteria, (b) urease, (c) $Ca^{2+}$, and (d) solute $CaCO_3$.

at the end of day 1. On day 2, the initial concentrations of bacteria and $Ca^{2+}$ are thus updated to $(10^8 + 5.35 \times 10^7)/2 = 7.68 \times 10^7$ cell/mL and $0.25/2 = 0.125$ mol/L, respectively. The concentration of solute $CaCO_3$ increases from 0 to a plateau of 0.125 mol/L within 3 h. The time required to reach the plateau concentration is shorter than that of day 1, because the concentration of urease is higher than the corresponding time on day 1 (Fig. 9b). Thereafter on each day from 3–10, the concentration of solute $CaCO_3$ increases from 0 to the plateau of 0.125 mol/L within 1 h. As shown in Fig. 9d, the concentration of solute $CaCO_3$ during the majority time of day 2–10 can be approximated as

$$C_c = \frac{C^0_{Ca^{2+}}}{2} \tag{28}$$

Note that Eq. (28) is valid only under the following three conditions: (1) $C^0_{urea} > C^0_{Ca^{2+}}$; (2) the half volume of the old precipitation medium will be refreshed with the new precipitation medium every 24 h (a day); and (3) the initial concentration of bacteria $C^0_{bacteria}$ is high enough to enable a rapid increasing of the concentration of solute $CaCO_3$ to the plateau within a very short time after day 1.

### 4.2. Bridged pillar: radius and length

From day 2, the concentration of solute $CaCO_3$ can be approximated as $C_c = C^0_{Ca^{2+}}/2$. With Eq. (17), we can obtain the analytical solution for the pillar radius, written as

$$r = \sqrt{\frac{DC^0_{Ca^{2+}} t}{C_p\left(1 + \sqrt{\frac{4C_p - C^0_{Ca^{2+}}}{C^0_{Ca^{2+}}}}\right)}} \tag{29}$$

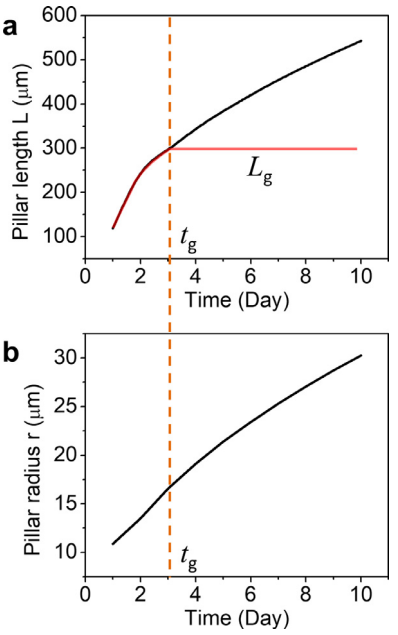


**Fig. 10.** Theoretically calculated(a) pillar length and (b) radius in functions of healing time.

Using Eq. (19), we can also obtain the analytical solution for the pillar length, calculated as

$$L = \frac{D\left(2C_p - C^0_{Ca^{2+}}\right)}{2C^0_{Ca^{2+}}}\sqrt{\frac{C_p\left(1+\sqrt{\frac{4C_p - C^0_{Ca^{2+}}}{C^0_{Ca^{2+}}}}\right)t}{DC^0_{Ca^{2+}}}} \tag{30}$$

When $L = L_g$, the crystal pillars begin to bridge the fracture interface. The corresponding time $t_g$ can be calculated as

$$t_g = \frac{L_g^2}{\left[\frac{D\left(2C_p - C^0_{Ca^{2+}}\right)}{2C^0_{Ca^{2+}}}\right]^2 \frac{C_p\left(1+\sqrt{\frac{4C_p - C^0_{Ca^{2+}}}{C^0_{Ca^{2+}}}}\right)}{DC^0_{Ca^{2+}}}} \tag{31}$$

With adequate parameters (Table 1), we present the theoretically calculated results for the pillar length and radius in Fig. 10. As shown in Fig. 10a, when $L_g = 300\mu$m (used in the experiment), $t_g = 3$ day. It means that no crystal pillars bridge the fracture interface before day 3 and the corresponding interfacial bonding is also zero. After $t_g$, the length of the bridged pillars does not change anymore (Fig. 10a), but their radii keep increasing approximately following Eq. (29) (Fig. 10b).

### 4.3. Evolution of interfacial healing strength

To calculate the interfacial healing strength, we need the following three steps: We first using the chemical kinetics to obtain the plateau bacterial concentration on days 2–10. With the adequate parameters, we obtain $C^p_{bacteria} \approx 5.74 \times 10^7$ cell/mL. Then, using Eqs. (9), (22), and (29), we calculate the area of the bridged pillars per unit interface area as

$$A(t) = \frac{\pi DC^0_{Ca^{2+}} k_u C^p_{bacteria}}{2C_p\left(1+\sqrt{\frac{4C_p - C^0_{Ca^{2+}}}{C^0_{Ca^{2+}}}}\right)}\left(t^2 - t_g^2\right) \tag{32}$$

when $A(t) = 1$, the time is calculated as

$$t_1 = \sqrt{\frac{2C_p\left(1+\sqrt{\frac{4C_p - C^0_{Ca^{2+}}}{C^0_{Ca^{2+}}}}\right)}{\pi DC^0_{Ca^{2+}} k_u C^p_{bacteria}} + t_g^2} \tag{33}$$

Note that Eq. (32) is only used for $t_g \le t \le t_1$. When $t < t_g$, $A(t) = 0$; and when $t > t_1$, $A(t) = 1$. With adequate parameters (Table 1), the theoretically calculated $A(t)$ is plotted in Fig. 11a. Then, with given $E_0$ and $S_0$ that are used in

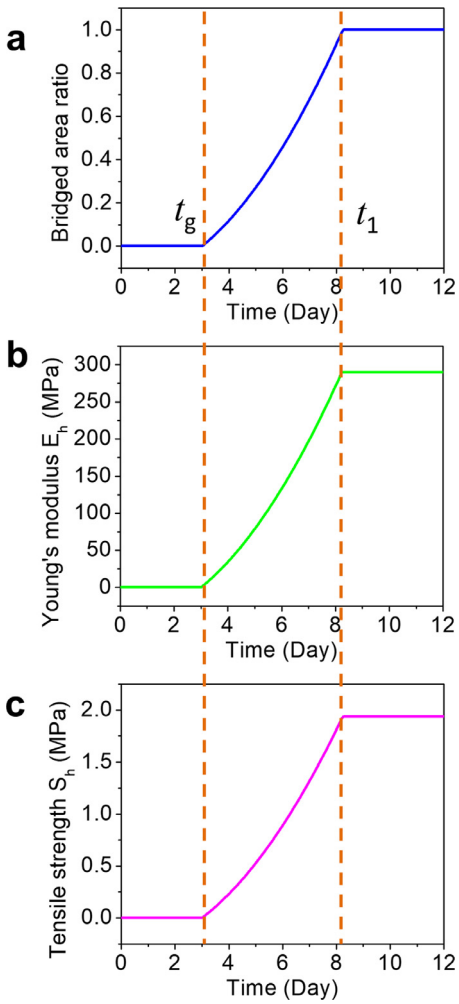


**Fig. 11.** Theoretically calculated (a) bridged area ratio, (b) effective Young's modulus and (c) effective tensile strength of the cohesive zone in functions of healing days.

Eqs. (26) and (27), we can plot the theoretically calculated tensile strength $S_h$ and Young's modulus $E_h$ of the healed cohesive zone, shown in Fig. 11bc, respectively.

With the property parameters of the healed cohesive zone and the parent material (Table 1), we can carry out the simulations for the cohesive fractures under three-point bending using a finite element package, ABAQUS 6.14 (Fig. 8a). 2D plane-stress models with three parts (two ceramic parts and the center cohesive element) were constructed. Bilinear traction-separation laws were employed to model the cohesive zone elements (Fig. 8b). Quadratic stress criterion was used to determine the damage initiation (Eq. (25)). We employed CPS4R elements to model the ceramic parts and COH2D4 elements to model the cohesive zone. Simulation accuracy was ensured through a mesh refinement study. Representative simulations for the samples on days 4, 6, 8 and 10 are shown in Fig. 12a-d. As shown in the simulations, the critical displacement of the denting load for the fracture initiation is zero before day 3, and then increases to a plateau after $t = 8.25$ day (Fig. 12e). For the samples on each day after day 3, the applied load initially increases with the increasing displacement, and then drastically decreases after a critical load $F_c$ (Fig. 12f). With the dimension of the three-point bending tests, we can calculate the flexural strength of the healed interface as

$$\sigma_h = \frac{3F_cL_s}{2wd} \tag{34}$$

where $L_s$ is the length of the support span, $w$ is the sample width, and $d$ is the sample thickness. If we denote the flexural strength of the virgin sample as $\sigma_0$, the healing strength ratio can be defined as

$$\eta = \frac{\sigma_h}{\sigma_0} \tag{35}$$

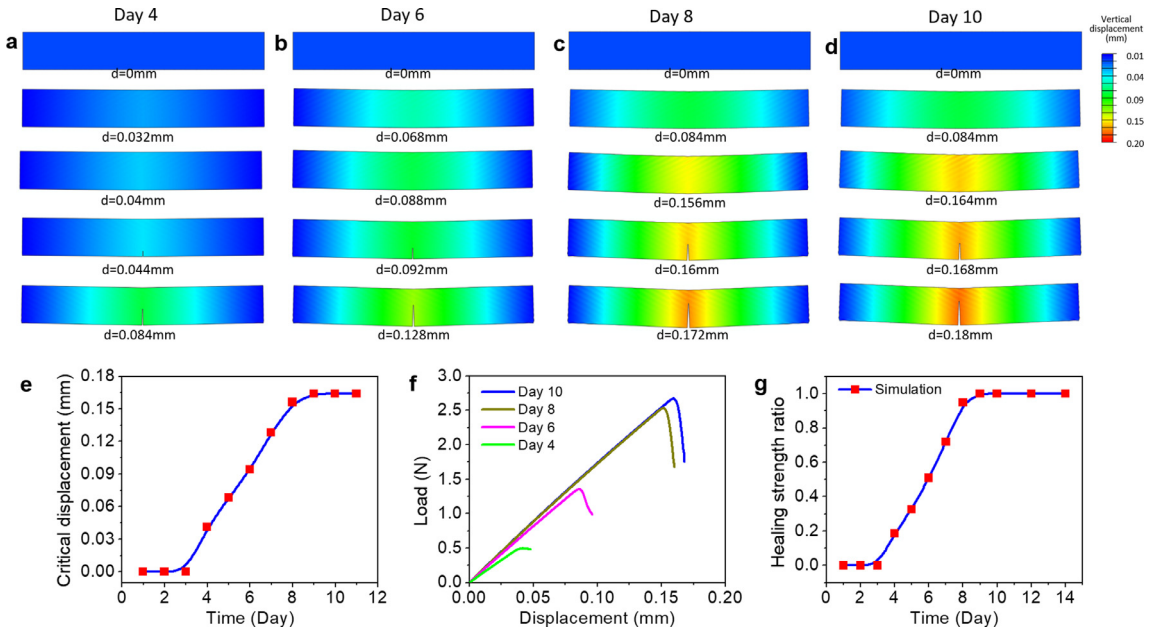


**Fig. 12.** (a-d) Simulations for the three-point-bending of the healed samples on healing days 4, 6, 8, and 10. (e) Critical displacement of the denting load for the crack initiation in a function of healing time. (f) Load-displacement relationships of the three-point-bending tests of healed samples on healing days 4, 6, 8, and 10. (g) The numerically simulated healing strength ratio in a function of healing time.

As shown in Fig. 12g, the healing strength ratio increases after $t_g = 3$ day, and then reaches the plateau of 1 after $t =$ 8.25 day. The healing strength ratio cannot be larger than 1 in the theoretical calculation, because the fracture will occur outside of the healing interface if the healing interface is stronger than the parament material; therefore, the overall flexural strength cannot be larger than the flexural strength of the parament material. To facilitate the following discussion, we further define the healing time corresponding to $\eta = 90\%$ as the equilibrium healing time, denoted as $t_{eq}$.

### *4.4. Effect of parameters on the healed interfacial strength*

In this section, we will discuss the effect of three parameters on the healing performance: fracture interface distance, initial concentration of bacteria, and initial concentration of calcium ions.

#### *4.4.1. Effect of fracture interface distance*

As the fracture interface distance $L_g$ increases, the required minimal time $t_g$ to enable non-zero healing strength increases quadratically (Eq. (31), Fig. 13a). Subsequently, the bridged area ratio $A(t)$ and the healing strength ratio $\eta$ for various interface distances can be calculated and plotted in Fig. 13b and c, respectively. Then, the equilibrium healing time $t_{eq}$ corresponding to 90% healing for various interface distances is shown in Fig. 13d. As shown in Fig. 13d, $t_{eq}$ increases with increasing interface distance $L_g$, because larger distance requires a longer time to bridge the fracture interface. Besides, we find that $t_{eq}$ cannot decrease to a very small value but reaches a plateau as the interface distance $L_g$ deceases. The plateau equilibrium healing time is around 7.3 days.

#### *4.4.2. Effect of the initial concentration of bacteria*

For different initial concentrations of bacteria $C^0_{bacteria}$, the plateau bacterial concentration $C^p_{bacteria}$ can be first calculated. Then, the bridged area ratio $A(t)$ and the healing strength ratio $\eta$ can be calculated and plotted in Fig. 14a and b, respectively. Since $L_g$ and $C^0_{Ca^{2+}}$ are unchanged, the minimal healing time $t_g$ is unchanged. However, the equilibrium healing time $t_{eq}$ decreases with the increasing initial bacterial concentrations (Fig. 14c), because higher concentration of the bacteria enables higher rates of crystal nucleation and growth.

#### *4.4.3. Effect of the initial concentration of calcium ions*

Revealed from Eq. (29), the pillar radius increases with increasing initial concentrations of $Ca^{2+}$ (Fig. 15a). However, revealed from Eq. (30), the pillar length decreases with increasing initial concentrations of $Ca^{2+}$ (Fig. 15b). This is probably because that the pillar with smaller radius tends to grow easier. With the calculated pillar radius and length, the bridged area ratio $A(t)$, the healing strength ratio $\eta$, and the corresponding equilibrium healing time $t_{eq}$ can be calculated and plotted in Fig. 15c-e, respectively. Because the reverse trends of the pillar radius and length, the equilibrium healing time $t_{eq}$ first decreases and then increases with increasing $C^0_{Ca^{2+}}$. The first decreasing is because that the higher $C^0_{Ca^{2+}}$ leads to larger pillar

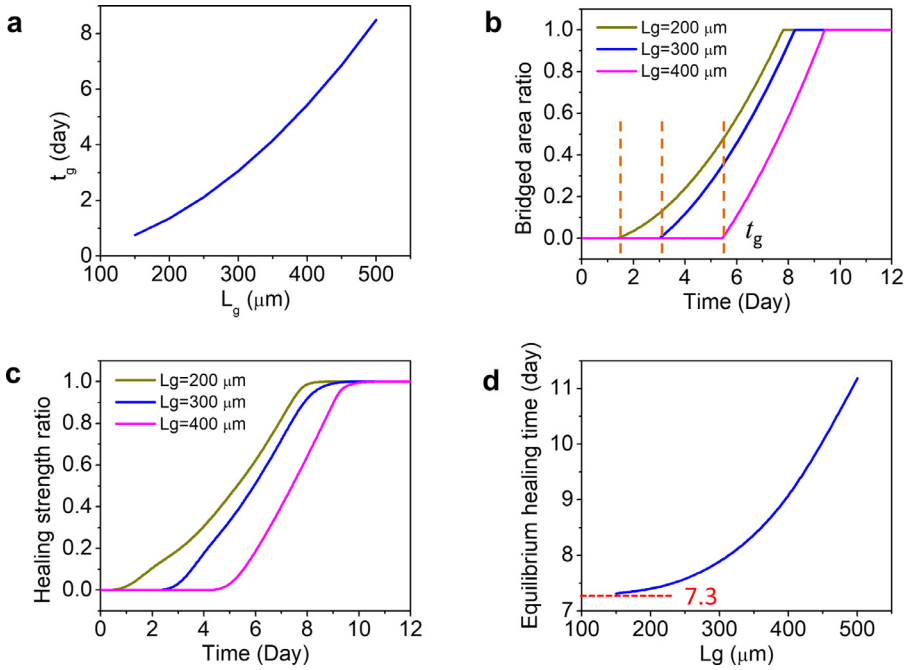


**Fig. 13.** Effect of the fracture interface distance. (a) The minimal time for interfacial bridging $t_g$ in a function of the fracture interface distance $L_g$. (b) The bridged area ratios for various interface distances in functions of time. (c) The healing strength ratios for various interface distances in functions of time. (d) The equilibrium healing time in a function of the interface distance.

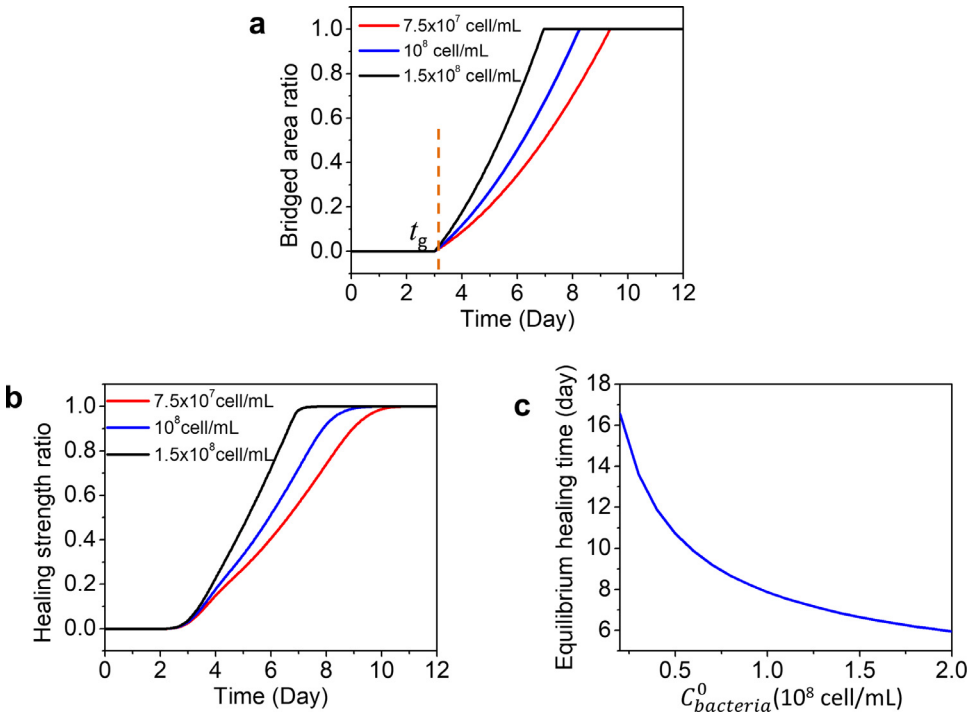


**Fig. 14.** Effect of the initial bacterial concentration. (a) The bridged area ratios for various initial bacterial concentrations in functions of time. (b) The healing strength ratios for various initial bacterial concentrations in functions of time. (c) The equilibrium healing time in a function of the initial bacterial concentration.

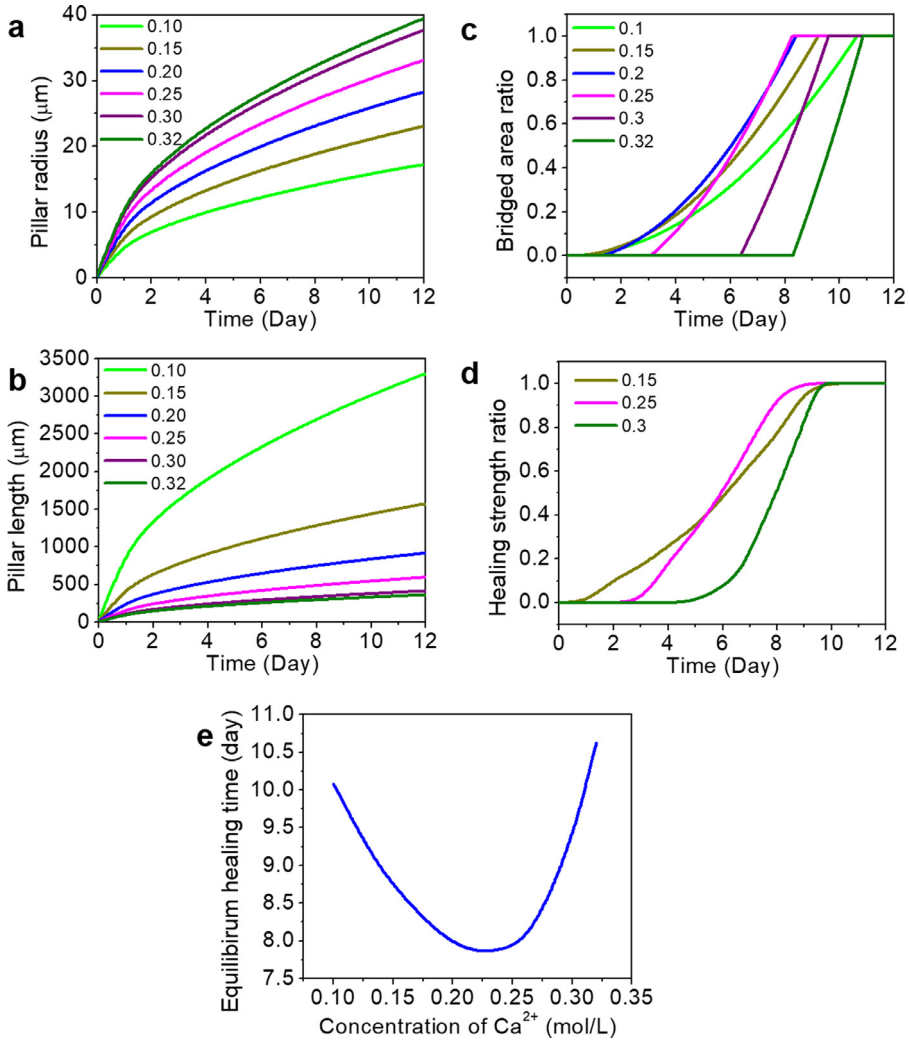


**Fig. 15.** Effect of the initial $Ca^{2+}$concentration. (a) The pillar radii and (b) length for various initial $Ca^{2+}$concentrations in functions of time. (c) The bridged area ratios and (d) The healing strength ratios for various initial $Ca^{2+}$concentrations in functions of time. (e) The equilibrium healing time in a function of the initial $Ca^{2+}$concentration.

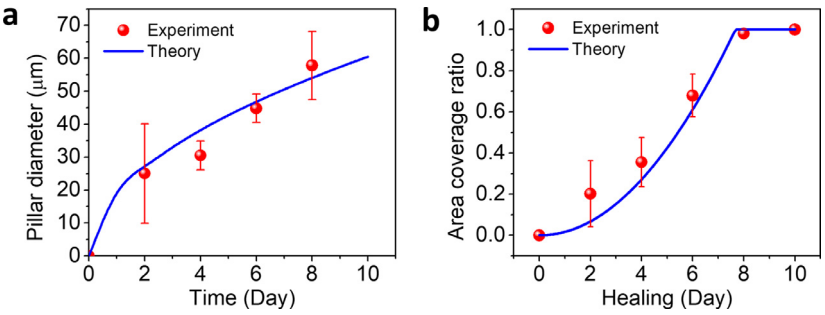


**Fig. 16.** Comparison with experimentally measured results of crystal precipitations. (a) The experimentally measured and theoretically calculated pillar diameters in functions of time. (b) The experimentally measured and theoretically calculated covered area ratios in functions of time.

radius; the latter increasing is because that too high $C^0_{Ca^{2+}}$ induces a reduced pillar growth length. The initial concentration of $Ca^{2+}$ corresponding to smallest equilibrium healing time is around 0.2–0.26 mol/L. The employed initial concentration of $Ca^{2+}$ used in the experiment is $C^0_{Ca^{2+}} = 0.25\ mol/L$.

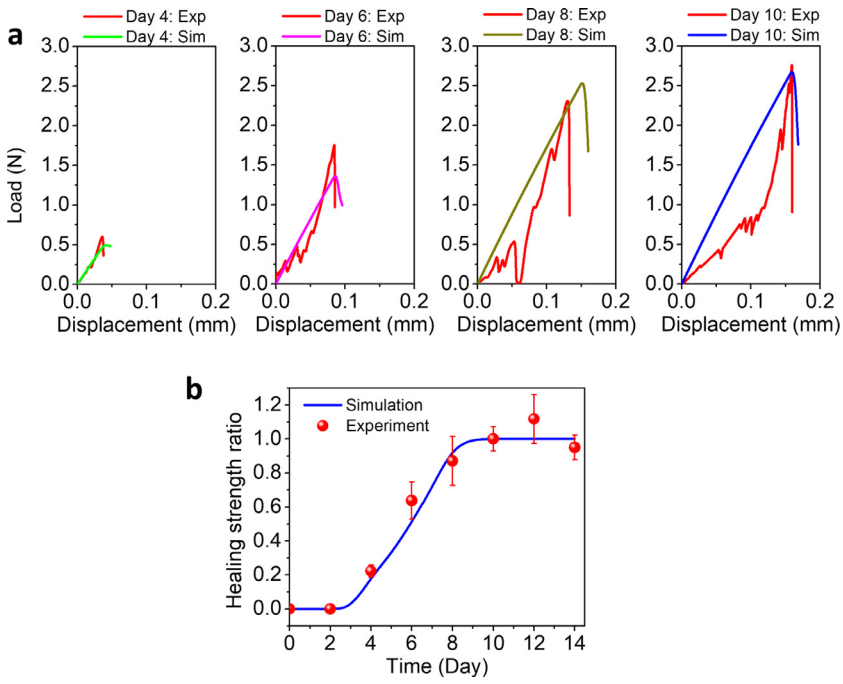


**Figure 17.** Comparison with experimental results on bacteria-assisted healing of ceramics. (a) The experimentally measured and theoretically calculated load-displacement curves for healed samples on healing days 4, 6, 8, and 10. (b) The experimentally measured and theoretically calculated healing strength ratios in functions of time.

## 5. Comparison with experiments

### 5.1. Compared with ceramic experiments

We here first compare the modeling results with the experiments on ceramics. From the SEM images of the fractured interfaces of the healed samples for various healing days, we roughly measured the diameters ($2r$) and the covered area ratios of the crystals (Fig. 16ab). From Eq. (29), we can plot the theoretically calculated pillar diameters which roughly agree with the experimentally measured results (Fig. 16a). Besides, the covered area ratio can be calculated using

$$A_c(t) = \int_0^t \dot{N}_{net}(t-\tau)\pi r^2(\tau)d\tau \tag{36}$$

Using Eqs. (9) and 29, the covered area ratio can be formulated as

$$A_c(t) = \frac{\pi D C^0_{Ca^{2+}} k_u C^p_{bacteria}}{2C_p\left(1+\sqrt{\frac{4C_p - C^0_{Ca^{2+}}}{C^0_{Ca^{2+}}}}\right)} t^2 \tag{37}$$

Note that $A_c(t)$ is different from $A(t)$ because non-bridged crystal pillars can also be counted in $A_c(t)$. Different from $A(t)$, $A_c(t)$ increases from zero at time $t = 0$. After $A_c(t) = 1$, $A_c(t)$ will remain at the plateau of 1. The theoretically calculated $A_c(t)$ is plotted in Fig. 16b, which shows that the theoretically calculated covered area ratio roughly agrees with the experimental results. The comparisons shown in Fig. 16 verify that the proposed model can roughly explain the crystal precipitation within the fracture interface.

Next, we examine if the proposed model can explain the mechanical properties of the three-point bending tests. Fig. 17a shows the direct comparison between the numerically calculated load-displacement curves and the corresponding experimental results of the three-point bending tests on healed samples for various healing days. The numerically calculated results can capture the trend of the load-displacement curves, while the experimentally measured load-displacement curves are more complex. It is probably because that the bacteria-assisted precipitation of crystals may be more complex than merely pillar shape. However, the numerically calculated effective healing strength ratios for various healing days are consistent with the experimental results (Fig. 17b). This implies that though the assumed crystal growth geometry in the proposed model may be not fully correct to reveal the real crystal geometry on the healing interface, the overall mechanics behavior of the crystal-precipitation-enabled healing can be well captured.

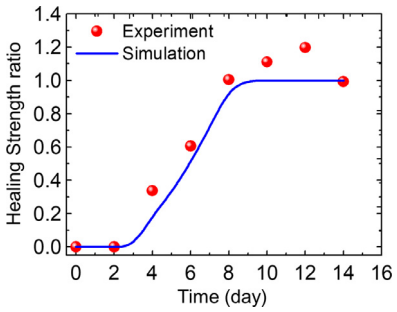


**Fig. 18.** Comparison with experimental results on bacteria-assisted healing of cement. The experimentally measured and theoretically calculated healing strength ratio in a function of time.

### *5.2. Compared with cement experiments*

To further verify the proposed model, we employ the proposed model to explain the crystal-precipitation-enabled healing of fractured cement (Figs. 4 and 18). We use the same experimental condition to enable the interfacial healing of fractured cement. Overall, the experimentally measured healing strengths for various healing days are very similar to those of the ceramics. Our model system can roughly explain the relationship between the healing strength ratio and the healing day (Fig. 18). It shows that the proposed model may be helpful for explaining the existing experiments on microorganism-assisted healing of cementitious materials (Achal and Mukherjee, 2015; Jonkers et al., 2010; Luo et al., 2018; Nguyen et al., 2018; Wang et al., 2014).

## 6. Conclusive remarks

In summary, taking bacterial-precipitation-enabled healing as an example, we construct a modeling framework to explain the extrinsic healing mechanics. We develop a model for the growth of crystal pillars to explain the bacteria-assisted growth of the $CaCO_3$ precipitation within the fracture interface, and a cohesive zone model to explain the interfacial bonding. Our modeling framework can explain the evolution of the interfacial healing strength over the healing time. The modeling results are consistent with the bacteria-assisted healing experiments of ceramics and cement. We expect this model system can be further extended to explain other precipitation-enabled extrinsic healing processes.

Note that the present model system is totally different from the model systems for the intrinsic healing mechanics proposed by Wang et al. (2017), Xin et al. (2019), Yu et al. (2019a, 2018, 2019b). As the first-generation model for the extrinsic healing mechanics, the current model system is highly simplified to avoid complex computations. First, adequate initial concentrations of bacteria, urea, and calcium ions are given to enable an approximately constant concentration of the solute $CaCO_3$ after day 1. This condition significantly simplifies the calculation of the crystal pillar diameter and length. Second, the crystal is modeled as a pillar that bridges the fracture interface. From the SEM images in Fig. 3c, this assumption can only partially capture the physics. Third, the growth of each pillar is assumed as an independent behavior. As shown in the SEM images in Fig. 3c, adjacent pillars may intensively interact during the growth process. Our assumption of independent growth can drastically reduce the complexity of the problem. Fourth, here we only focus on strain crack propagation, but the proposed healing model can be extended to explain other fracture geometries. Finite element models with the cohesive zone elements can be used to simulate the crack propagation for other fracture geometries.

As mentioned earlier, the proposed mechanism may be used to heal 3D-printed ceramics. The application in healing 3D-printed ceramics may be achieved through two possible routes: (A) If the 3D-printed ceramic structure is broken into two parts, they can be brought into contact with a small interfacial gap (e.g., 300 μm), and then healed by bacteria-assisted crystal precipitation. (B) The bacterial and precipitation media can also be pre-filled in the ceramic pores. If there are cracks or damages, the precipitated crystals can fill the crack space to autonomously restore the mechanical strength. In addition, compared to intrinsically healable polymers whose healing time is typically in the order of hours (Binder, 2013; Li et al., 2018; Roy et al., 2015; Taylor, 2016; Thakur and Kessler, 2015; van der Zwaag, 2007; Wei et al., 2014; Wojtecki et al., 2011; Wu et al., 2008; Yang and Urban, 2013), the crystal-precipitation-enabled healing shown in this paper requires several days. This time scale is because of the slow process of the crystal nucleation and growth. On the other hand, the healing of a fractured human bone relies on stem cells called *osteoblasts* to precipitate mineralized calluses (primarily $Ca_{10}(PO_4)_6(OH)_2$) to bridge fracture interfaces (Guan et al., 2012; Schindeler et al., 2008; Taylor et al., 2007). Compared to the callus-precipitation-enabled repairing of human bones that typically requires months (Guan et al., 2012; Schindeler et al., 2008; Taylor et al., 2007), the time scale for the bacteria-assisted healing of ceramics is acceptable.

## Declaration of Competing Interest

The authors declare the following financial interests/personal relationships which may be considered as potential competing interests:

The University of Southern California has filed a patent application related to the bacteria-assisted healing demonstrated in this work.

## CRediT authorship contribution statement

**An Xin:** Conceptualization, Methodology, Formal analysis, Data curation, Writing - original draft, Investigation, Resources. **Haixu Du:** Investigation, Resources. **Kunhao Yu:** Investigation, Resources. **Qiming Wang:** Conceptualization, Methodology, Formal analysis, Data curation, Writing - original draft, Supervision, Project administration.

## Acknowledgement

The authors acknowledge the funding support from the National Science Foundation (CMMI-1762567) and the Air Force Office of Scientific Research Young Investigator Program (FA9550-18-1-0192, program manager: Dr. Ming-Jen Pan).

## Supplementary materials

Supplementary material associated with this article can be found, in the online version, at doi:10.1016/j.jmps.2020.103938.

## Reference

Achal, V., Mukherjee, A., 2015. A review of microbial precipitation for sustainable construction. Construct. Build. Mater. 93, 1224–1235.
Ando, K., Chu, M.-.C., Tsuji, K., Hirasawa, T., Kobayashi, Y., Sato, S., 2002. Crack healing behaviour and high-temperature strength of mullite/SiC composite ceramics. J. Eur. Ceram. Soc. 22, 1313–1319.
Ando, K., Furusawa, K., Chu, M.C., Hanagata, T., Tuji, K., Sato, S., 2001. Crack-Healing behavior under stress of mullite/silicon carbide ceramics and the resultant fatigue strength. J. Am. Ceram. Soc. 84, 2073–2078.
Balluffi, R.W., Allen, S., Carter, W.C., 2005. Kinetics of Materials. John Wiley & Sons.
Bang, S.S., Galinata, J.K., Ramakrishnan, V., 2001. Calcite precipitation induced by polyurethane-immobilized bacillus pasteurii. Enzyme Microb. Technol. 28, 404–409.
Barry, Z.T., 2018. Mathematical and computational considerations of a model of microbiologically induced calcite precipitation.
Binder, W.H., 2013. Self-healing polymers: from Principles to Applications. John Wiley & Sons.
Blaiszik, B., Kramer, S., Olugebefola, S., Moore, J.S., Sottos, N.R., White, S.R., 2010. Self-healing polymers and composites. Annu. Rev. Mater. Res. 40, 179–211.
Brochu, A.B., Craig, S.L., Reichert, W.M., 2011. Self-healing biomaterials. J. Biomed. Mater. Res. Part A 96, 492–506.
Burnworth, M., Tang, L., Kumpfer, J.R., Duncan, A.J., Beyer, F.L., Fiore, G.L., Rowan, S.J., Weder, C., 2011. Optically healable supramolecular polymers. Nature 472, 334.
Chen, X., Dam, M.A., Ono, K., Mal, A., Shen, H., Nutt, S.R., Sheran, K., Wudl, F., 2002. A thermally re-mendable cross-linked polymeric material. Science 295, 1698–1702.
Chen, Y., Kushner, A.M., Williams, G.A., Guan, Z., 2012. Multiphase design of autonomic self-healing thermoplastic elastomers. Nat. Chem. 4, 467–472.
Cho, S.H., Andersson, H.M., White, S.R., Sottos, N.R., Braun, P.V., 2006. Polydimethylsiloxane-based self-healing materials. Adv. Mater. 18, 997–1000.
Chu, M., Sato, S., Kobayashi, Y., Ando, K., 1995. Damage healing and strengthening behaviour in intelligent mullite/SiC ceramics. Fatigue Fract. Eng. Mater. Struct. 18, 1019–1029.
Cordier, P., Tournilhac, F., Soulié-Ziakovic, C., Leibler, L., 2008. Self-healing and thermoreversible rubber from supramolecular assembly. Nature 451, 977–980.
Das, A., Sallat, A., Böhme, F., Suckow, M., Basu, D., Wießner, S., Stöckelhuber, K.W., Voit, B., Heinrich, G., 2015. Ionic modification turns commercial rubber into a self-healing material. ACS Appl. Mater. Interfaces 7, 20623–20630.
De Muynck, W., De Belie, N., Verstraete, W., 2010. Microbial carbonate precipitation in construction materials: a review. Ecol. Eng. 36, 118–136.
Ebigbo, A., Phillips, A., Gerlach, R., Helmig, R., Cunningham, A.B., Class, H., Spangler, L.H., 2012. Darcy-scale modeling of microbially induced carbonate mineral precipitation in sand columns. Water Resour. Res. 48, W07519. doi:10.1029/2011WR011714.
Eckel, Z.C., Zhou, C., Martin, J.H., Jacobsen, A.J., Carter, W.B., Schaedler, T.A., 2016. Additive manufacturing of polymer-derived ceramics. Science 351, 58–62.
Elices, M., Guinea, G., Gomez, J., Planas, J., 2002. The cohesive zone model: advantages, limitations and challenges. Eng. Fract. Mech. 69, 137–163.
Fox, J., Wie, J.J., Greenland, B.W., Burattini, S., Hayes, W., Colquhoun, H.M., Mackay, M.E., Rowan, S.J., 2012. High-strength, healable, supramolecular polymer nanocomposites. J. Am. Chem. Soc. 134, 5362–5368.
Ghosh, B., Urban, M.W., 2009. Self-repairing oxetane-substituted chitosan polyurethane networks. Science 323, 1458–1460.
Gibson, L.J., Ashby, M.F., 1999. Cellular Solids: Structure and Properties. Cambridge university press.
Grodzinsky, A.J., 2011. Fields, Forces, and Flows in Biological Systems. Garland Science.
Guan, M., Yao, W., Liu, R., Lam, K.S., Nolta, J., Jia, J., Panganiban, B., Meng, L., Zhou, P., Shahnazari, M., 2012. Directing mesenchymal stem cells to bone to augment bone formation and increase bone mass. Nat. Med. 18, 456.
Gulyuz, U., Okay, O., 2014. Self-Healing poly (acrylic acid) hydrogels with shape memory behavior of high mechanical strength. Macromolecules 47, 6889–6899.
Halloran, J.W., 2016. Ceramic stereolithography: additive manufacturing for ceramics by photopolymerization. Annu. Rev. Mater. Res. 46, 19–40.
Haraguchi, K., Uyama, K., Tanimoto, H., 2011. Self-healing in nanocomposite hydrogels. Macromol. Rapid Commun. 32, 1253–1258.
Hillert, M., 1957. The role of interfacial energy during solid-state phase transformations. Jernkontorets Annaler 141, 757–789.
Holten-Andersen, N., Harrington, M.J., Birkedal, H., Lee, B.P., Messersmith, P.B., Lee, K.Y.C., Waite, J.H., 2011. pH-induced metal-ligand cross-links inspired by mussel yield self-healing polymer networks with near-covalent elastic moduli. Proc. Natl. Acad. Sci. USA 108, 2651–2655.
Hommel, J., Lauchnor, E., Phillips, A., Gerlach, R., Cunningham, A.B., Helmig, R., Ebigbo, A., Class, H., 2015. A revised model for microbially induced calcite precipitation: improvements and new insights based on recent experiments. Water Resour. Res 51, 3695–3715.
Ihsan, A.B., Sun, T.L., Kurokawa, T., Karobi, S.N., Nakajima, T., Nonoyama, T., Roy, C.K., Luo, F., Gong, J.P., 2016. Self-Healing behaviors of tough polyampholyte hydrogels. Macromolecules 49, 4245–4252.
Imato, K., Nishihara, M., Kanehara, T., Amamoto, Y., Takahara, A., Otsuka, H., 2012. Self-healing of chemical gels cross-linked by diarylbibenzofuranone-based trigger-free dynamic covalent bonds at room temperature. Angew. Chem. Int. Ed. 51, 1138–1142.

Jang, D., Meza, L.R., Greer, F., Greer, J.R., 2013. Fabrication and deformation of three-dimensional hollow ceramic nanostructures. Nat. Mater. 12, 893.
Johnson, K.A., Goody, R.S., 2011. The original Michaelis constant: translation of the 1913 Michaelis–Menten paper. Biochemistry 50, 8264–8269.
Jonkers, H.M., Thijssen, A., Muyzer, G., Copuroglu, O., Schlangen, E., 2010. Application of bacteria as self-healing agent for the development of sustainable concrete. Ecol. Eng. 36, 230–235.
Juška, A., Gedminienė, G., Ivanec, R., 2006. Growth of microbial populations. mathematical modeling, laboratory exercises, and model-based data analysis. Biochem. Mol. Biol. Educ. 34, 417–422.
Keller, M.W., White, S.R., Sottos, N.R., 2007. A self-healing poly (Dimethyl siloxane) elastomer. Adv. Funct. Mater. 17, 2399–2404.
Kersey, F.R., Loveless, D.M., Craig, S.L., 2007. A hybrid polymer gel with controlled rates of cross-link rupture and self-repair. J. R. Soc. Interface 4, 373–380.
Krajewska, B., 2009. Ureases I. Functional, catalytic and kinetic properties: a review. J. Mol. Catal. B: Enzymatic 59, 9–21.
Li, H., Xiao, H.-g., Yuan, J., Ou, J., 2004. Microstructure of cement mortar with nano-particles. Compos. Part B: Eng. 35, 185–189.
Li, S., Song, G., Kwakernaak, K., van der Zwaag, S., Sloof, W.G., 2012. Multiple crack healing of a Ti2AlC ceramic. J. Eur. Ceram. Soc. 32, 1813–1820.
Li, W., Dong, B., Yang, Z., Xu, J., Chen, Q., Li, H., Xing, F., Jiang, Z., 2018. Recent advances in intrinsic self-healing cementitious materials. Adv. Mater 30, 1705679.
Li, W., Liu, J., Zhao, D., 2016. Mesoporous materials for energy conversion and storage devices. Nat. Rev. Mater. 1, 16023.
Liu, J., Tan, C.S.Y., Yu, Z., Lan, Y., Abell, C., Scherman, O.A., 2017a. Biomimetic supramolecular polymer networks exhibiting both toughness and self-recovery. Adv. Mater. 29, 1604951.
Liu, J., Tan, C.S.Y., Yu, Z., Li, N., Abell, C., Scherman, O.A., 2017b. Tough supramolecular polymer networks with extreme stretchability and fast room-temperature self-healing. Adv. Mater. 29, 1605325.
Low, Z.-.X., Chua, Y.T., Ray, B.M., Mattia, D., Metcalfe, I.S., Patterson, D.A., 2017. Perspective on 3D printing of separation membranes and comparison to related unconventional fabrication techniques. J. Memb. Sci. 523, 596–613.
Lu, Y.-.X., Guan, Z., 2012. Olefin metathesis for effective polymer healing via dynamic exchange of strong carbon–carbon double bonds. J. Am. Chem. Soc. 134, 14226–14231.
Luo, J., Chen, X., Crump, J., Zhou, H., Davies, D.G., Zhou, G., Zhang, N., Jin, C., 2018. Interactions of fungi with concrete: significant importance for bio-based self-healing concrete. Construct. Build. Mater. 164, 275–285.
Mayumi, K., Guo, J., Narita, T., Hui, C.Y., Creton, C., 2016. Fracture of dual crosslink gels with permanent and transient crosslinks. Extreme Mech. Lett. 6, 52–59.
Meza, L.R., Das, S., Greer, J.R., 2014. Strong, lightweight, and recoverable three-dimensional ceramic nanolattices. Science 345, 1322–1326.
Montarnal, D., Tournilhac, F., Hidalgo, M., Couturier, J.-.L., Leibler, L., 2009. Versatile one-pot synthesis of supramolecular plastics and self-healing rubbers. J. Am. Chem. Soc. 131, 7966–7967.
Muth, J.T., Dixon, P.G., Woish, L., Gibson, L.J., Lewis, J.A., 2017. Architected cellular ceramics with tailored stiffness via direct foam writing. Proc. Natl. Acad. Sci. 114, 1832–1837.
Nakahata, M., Takashima, Y., Yamaguchi, H., Harada, A., 2011. Redox-responsive self-healing materials formed from host–guest polymers. Nat. Comm. 2, 511.
Nguyen, P.Q., Courchesne, N.D., Duraj-Thatte, A., Praveschotinunt, P., Joshi, N.S., 2018. Engineered living materials: prospects and challenges for using biological systems to direct the assembly of smart materials. Adv. Mater. 30, e1704847.
Okay, O., 2015. Self-healing hydrogels formed via hydrophobic interactions. Supramolecular Polymer Networks and Gels. Springer, pp. 101–142.
Osada, T., Kamoda, K., Mitome, M., Hara, T., Abe, T., Tamagawa, Y., Nakao, W., Ohmura, T., 2017. A novel design approach for self-crack-healing structural ceramics with 3D networks of healing activator. Sci. Rep. 7, 17853.
Padture, N.P., Gell, M., Jordan, E.H., 2002. Thermal barrier coatings for gas-turbine engine applications. Science 296, 280–284.
Park, J., Lakes, R.S., 2007. Biomaterials: an Introduction. Springer Science & Business Media.
Phadke, A., Zhang, C., Arman, B., Hsu, C.-.C., Mashelkar, R.A., Lele, A.K., Tauber, M.J., Arya, G., Varghese, S., 2012. Rapid self-healing hydrogels. Proc. Natl. Acad. Sci. USA 109, 4383–4388.
Porter, D.A., Easterling, K.E., Sherif, M., 2009. Phase Transformations in Metals and Alloys, (Revised Reprint). CRC press.
Pugh, P.D.G., Pugh, M., 1971. Naval Ceramics. Ceramic Book Co.
Raj, S.V., Singh, M., Bhatt, R.T., 2014. High temperature lightweight self-healing ceramic composites for aircraft engine applications. NASA/TM—2014-218352.
Reddy, M., Gaillard, W., 1981. Kinetics of calcium carbonate (calcite)-seeded crystallization: influence of solid/solution ratio on the reaction rate constant. J. Colloid Interface Sci. 80, 171–178.
Rowan, S.J., Beck, J.B., 2005. Metal–ligand induced supramolecular polymerization: a route to responsive materials. Faraday Discuss. 128, 43–53.
Roy, N., Bruchmann, B., Lehn, J.-.M., 2015. DYNAMERS: dynamic polymers as self-healing materials. Chem. Soc. Rev. 44, 3786–3807.
Sarda, D., Choonia, H.S., Sarode, D., Lele, S., 2009. Biocalcification by bacillus pasteurii urease: a novel application. J. Ind. Microbiol. Biotechnol. 36, 1111–1115.
Schindeler, A., McDonald, M.M., Bokko, P., Little, D.G., 2008. Bone remodeling during fracture repair: the cellular picture. Seminars in Cell & Developmental Biology. Elsevier, pp. 459–466.
Sijbesma, R.P., Beijer, F.H., Brunsveld, L., Folmer, B.J., Hirschberg, J.K., Lange, R.F., Lowe, J.K., Meijer, E., 1997. Reversible polymers formed from self-complementary monomers using quadruple hydrogen bonding. Science 278, 1601–1604.
Skene, W.G., Lehn, J.-M.P., 2004. Dynamers: polyacylhydrazone reversible covalent polymers, component exchange, and constitutional diversity. Proc. Natl. Acad. Sci. USA 101, 8270–8275.
Sloof, W.G., Pei, R., McDonald, S.A., Fife, J.L., Shen, L., Boatemaa, L., Farle, A.-.S., Yan, K., Zhang, X., van der Zwaag, S., Lee, P.D., Withers, P.J., 2016. Repeated crack healing in MAX-phase ceramics revealed by 4D in situ synchrotron X-ray tomographic microscopy. Sci. Rep. 6, 23040.
Song, G.M., Pei, Y.T., Sloof, W.G., Li, S.B., De Hosson, J.T.M., van der Zwaag, S., 2008. Oxidation-induced crack healing in Ti3AlC2 ceramics. Scr. Mater. 58, 13–16.
Stocks-Fischer, S., Galinat, J.K., Bang, S.S., 1999. Microbiological precipitation of $CaCo_3$. Soil Biol. Biochem. 31, 1563–1571.
Sun, J.-.Y., Zhao, X., Illeperuma, W.R., Chaudhuri, O., Oh, K.H., Mooney, D.J., Vlassak, J.J., Suo, Z., 2012. Highly stretchable and tough hydrogels. Nature 489, 133–136.
Sun, T.L., Kurokawa, T., Kuroda, S., Ihsan, A.B., Akasaki, T., Sato, K., Haque, M.A., Nakajima, T., Gong, J.P., 2013. Physical hydrogels composed of polyampholytes demonstrate high toughness and viscoelasticity. Nat. Mater. 12, 932–937.
Taylor, D., Hazenberg, J.G., Lee, T.C., 2007. Living with cracks: damage and repair in human bone. Nat. Mater. 6, 263.
Taylor, D.L., 2016. Self-healing hydrogels. Adv. Mater 28, 9060–9093.
Tee, B.C., Wang, C., Allen, R., Bao, Z., 2012. An electrically and mechanically self-healing composite with pressure-and flexion-sensitive properties for electronic skin applications. Nat. Nanotechnol. 7, 825–832.
Tegethoff, F.W., Rohleder, J., Kroker, E., 2001. Calcium carbonate: from the Cretaceous period into the 21st Century. Springer Science & Business Media.
Teleken, J.T., Robazza, W.d.S., Gomes, G.d.A., 2011. Mathematical modeling of microbial growth in milk. Food Sci. Technol. 31, 891–896.
Terryn, S., Brancart, J., Lefeber, D., Van Assche, G., Vanderborght, B., 2017. Self-healing soft pneumatic robots. Sci. Robot. 2, eaan4268.
Thakur, V.K., Kessler, M.R., 2015. Self-healing polymer nanocomposite materials: a review. Polymer (Guildf) 69, 369–383.
Toohey, K.S., Sottos, N.R., Lewis, J.A., Moore, J.S., White, S.R., 2007. Self-healing materials with microvascular networks. Nat. Mater. 6, 581–585.
van der Zwaag, S., 2007. Self Healing Materials: An Alternative Approach to 20 Centuries of Materials Science. Springer Science & Business Media.
Wang, C., Liu, N., Allen, R., Tok, J.B.H., Wu, Y., Zhang, F., Chen, Y., Bao, Z., 2013a. A rapid and efficient self-healing thermo-reversible elastomer crosslinked with graphene oxide. Adv. Mater. 25, 5785–5790.
Wang, C., Wu, H., Chen, Z., McDowell, M.T., Cui, Y., Bao, Z., 2013b. Self-healing chemistry enables the stable operation of silicon microparticle anodes for high-energy lithium-ion batteries. Nat. Chem. 5, 1042–1048.
Wang, J.Y., Soens, H., Verstraete, W., De Belie, N., 2014. Self-healing concrete by use of microencapsulated bacterial spores. Cement Concr. Res. 56, 139–152.

Wang, Q., Gao, Z., Yu, K., 2017. Interfacial self-healing of nanocomposite hydrogels: theory and experiment. J. Mech. Phys. Solids 109, 288–306.
Wang, Q., Mynar, J.L., Yoshida, M., Lee, E., Lee, M., Okuro, K., Kinbara, K., Aida, T., 2010. High-water-content mouldable hydrogels by mixing clay and a dendritic molecular binder. Nature 463, 339–343.
Wei, Z., Yang, J.H., Zhou, J., Xu, F., Zrínyi, M., Dussault, P.H., Osada, Y., Chen, Y.M., 2014. Self-healing gels based on constitutional dynamic chemistry and their potential applications. Chem. Soc. Rev. 43, 8114–8131.
White, S.R., Sottos, N., Geubelle, P., Moore, J., Kessler, M.R., Sriram, S., Brown, E., Viswanathan, S., 2001. Autonomic healing of polymer composites. Nature 409, 794–797.
Wojtecki, R.J., Meador, M.A., Rowan, S.J., 2011. Using the dynamic bond to access macroscopically responsive structurally dynamic polymers. Nat. Mater. 10, 14–27.
Wu, D.Y., Meure, S., Solomon, D., 2008. Self-healing polymeric materials: a review of recent developments. Prog. Polym. Sci. 33, 479–522.
Xin, A., Zhang, R., Yu, K., Wang, Q., 2019. Mechanics of electrophoresis-induced reversible hydrogel adhesion. J. Mech. Phys. Solids 125, 1–21.
Yang, Y., Urban, M.W., 2013. Self-healing polymeric materials. Chem. Soc. Rev. 42, 7446–7467.
Yu, K., Xin, A., Du, H., Li, Y., Wang, Q., 2019a. Additive manufacturing of self-healing elastomers. NPG Asia Mater. 11, 7.
Yu, K., Xin, A., Wang, Q., 2018. Mechanics of self-healing polymer networks crosslinked by dynamic bonds. J. Mech. Phys. Solids 121, 408–431.
Yu, K., Xin, A., Wang, Q., 2019b. Mechanics of light-activated self-healing polymer networks. J. Mech. Phys. Solids 124, 643–662.
Zanchetta, E., Cattaldo, M., Franchin, G., Schwentenwein, M., Homa, J., Brusatin, G., Colombo, P., 2016a. Stereolithography of sioc ceramic microcomponents. Adv. Mater. 28, 370–376.
Zanchetta, E., Cattaldo, M., Franchin, G., Schwentenwein, M., Homa, J., Brusatin, G., Colombo, P., 2016b. Stereolithography of SiOC ceramic microcomponents. Adv. Mater. 28, 370–376.
Zener, C., 1946. Kinetics of the decomposition of austenite. Trans. Aime 167, 550–595.
Zener, C., 1949. Theory of growth of spherical precipitates from solid solution. J. Appl. Phys. 20, 950–953.
Zocca, A., Colombo, P., Gomes, C.M., Günster, J., 2015. Additive manufacturing of ceramics: issues, potentialities, and opportunities. J. Am. Ceram. Soc. 98, 1983–2001.
Zwietering, M., Jongenburger, I., Rombouts, F., Van't Riet, K., 1990. Modeling of the bacterial growth curve. Appl. Environ. Microbiol. 56, 1875–1881.